Deanship of Graduate Studies

Al-Quds University

Synthesis, Magnetic Properties, and Crystal Structures of Magnetocaloric Materials in the System $(Mn_5Ge_3)_x(MnFe_4Si_3)_{1-x}$

Kinan Khaled Jameel Al-Namourah

M.Sc. Thesis

Jerusalem – Palestine

1440 / 2019

Synthesis, Magnetic Properties, and Crystal Structures of Magnetocaloric Materials in the System $(\mathbf{Mn_5Ge_3})_x(\mathbf{MnFe_4Si_3})_{1-x}$

Kinan Khaled Jameel Al-Namourah
Physics Department, Al-Quds University, Palestine

Supervisor

Prof. Salman M. Salman
Physics Department, Al-Quds University, Palestine

Co-Supervisors

PD Dr. Karen Friese

Jülich Centre for Neutron Science-2, Forschungszentrum Jülich, Germany

Dr. Jörg Voigt

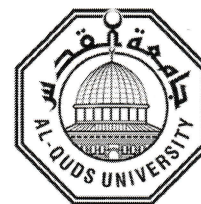Jülich Centre for Neutron Science-2, Forschungszentrum Jülich, Germany

A Thesis Submitted in Partial Fulfillment of the Requirements for the Degree of Master of Science in Physics, Faculty of Graduate Studies, at Al-Quds University

Jerusalem – Palestine
1440 / 2019

Al-Quds University

Deanship of Graduate Studies

Physics Program / Physics Department

Thesis Approval

Synthesis, magnetic properties and crystal structures of magnetocaloric materials in the system $(Mn_5Ge_3)_x(MnFe_4Si_3)_{1-x}$

Prepared by: Kinan Khaled Jameel Al-Namourah
Registration No.: 21612584

Supervisors:
Prof. Salman M. Salman, Physics Department, Al-Quds University, Palestine
PD Dr. Karen Friese, Jülich Centre for Neutron Science-2, FZJ, Germany
Dr. Jörg Voigt, Jülich Centre for Neutron Science-2, FZJ, Germany

Master thesis submitted and accepted, Date: 15/05/2019
The names and signatures of the examining committee members:

Head of Committee: Prof. Salman M. Salman   Signature: ...S. M. Salm...
Internal Examiner: Prof. Musa Abu Tair   Signature: ...M. B...
External Examiner: Prof. Mustafa Abu Safa   Signature: ....

Jerusalem - Palestine
1440 / 2019

Dedication

I lovingly dedicate this thesis to my great parents for their endless love, support and encouragement. To my sisters Reem and Sujoud. To my brothers Tammam and Qassam. To my nieces Raheeq and Rawasy.

Kinan Khaled Jameel Al-Namourah

Declaration

I, Kinan Khaled Al-Namourah, declare that this thesis "Synthesis, magnetic properties and crystal structures of magnetocaloric materials in the system $(Mn_5Ge_3)_x(MnFe_4Si_3)_{1-x}$" and the work presented in it are my own and have been generated by me as the result of my own original research and that they have not been submitted earlier elsewhere.

I confirm that this work was done under the supervision of Prof. Salman M. Salman from the Physics Department, Al-Quds University, Palestine, and PD Dr. Karen Friese from the Jülich Centre for Neutron Science-2 (JCNS-2), Forschungszentrum Jülich, Germany*.
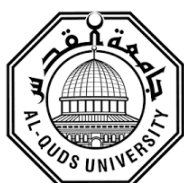
Kinan Khaled Jameel Al-Namourah

Jerusalem – Palestine
1440 / 2019

Acknowledgments

First of all, I wish to express my gratitude to the Almighty Allah for providing me the chance to make this thesis possible.

It is a pleasure to express my thanks and gratitude to everyone who supports, encourages and wishes the best for me.

I would like to thank my supervisor from Al-Quds University Prof. Salman M. Salman for his guidance during my university studies and providing the chance to conduct the practical part of this thesis within the framework collaboration between Al-Quds University and Research Centre Jülich.

Special thanks to my supervisors from Research Centre Jülich PD Dr. Karen Friese for her guidance, advices and improvement of my skills in writing; and Dr. Jörg Voigt for his assistance and the valuable discussions of the magnetization part which lead me to a better understanding. I extend my gratitude to Prof. Thomas Brückel for giving me the opportunity to perform the work in his institute.

Thanks to Jörg Persson for his help in preparing the samples. I would also like to express my deepest gratitude to the JCNS group for their kind support throughout my thesis work. They helped me to perform the measurements, and they were always helpful whenever I faced any problem, in particular I would like to thank Markus Herrmann for his help. I would also like to thank Dr. Volker Nischwitz from ZEA-3 for performing the chemical analysis.

Special appreciation for RWTH University to make the PW1050 diffractometer (MOPS) available to perform X-ray diffraction on my samples. I especially thank Marlies Reher for her help to do that.

Finally, my grateful thanks go to my parents, sisters and brothers for standing with me, providing the support when needed and calling Almighty Allah in their prayers to give me the highest level of success. Thanks to my extended family and my friends for their best wishes. Many thanks to anyone who taught me anything.

Kinan Khaled Jameel Al-Namourah

Abstract

The polycrystalline samples of several compositions in the system $(Mn_5Ge_3)_x(MnFe_4Si_3)_{1-x}$ with x = (0.2, 0.4, 0.6, 0.8) were prepared using cold crucible induction melting. Chemical analysis was performed using iCAP 7600 ICP-OES, in order to make sure that the synthesized compounds have the correct stoichiometry, and to confirm that the synthesize process was going well.

The crystal structures of these magnetocaloric compounds were investigated by performing X- ray powder diffraction using two types of diffractometers. Using the LeBail and Rietveld refinement, two main phases were detected in all samples. The volumes of the unit cell of the samples decrease with decreasing x parameter in the two phases. However, an unusually large value was observed at x = 0.2 for one of the phases. The polycrystalline samples x = 0.8 and 0.6 have a preferred orientation in the direction [0 0 1].

The magnetic properties of the compounds in the system $(Mn_5Ge_3)_x(MnFe_4Si_3)_{1-x}$ were investigated using a PPMS. Mass magnetization measurement as a function of temperature (isofield magnetization measurements) and magnetic field (isothermal magnetization measurements) were performed. The transition temperatures for all samples were different under field cooling compared to field warming. All samples showed a thermal hysteresis. The transitions were observed at temperatures slightly above the room temperature. The maximum transition was for the x = 0.6 composition at around 331 K for field cooling and around 337 K for field warming. From effective paramagnetic moment values, we conclude that we did not inter the Curie-Weiss regime.

Table of Contents

List of Tables

List of Figures

Chapter 5

Chapter 6

Appendix A Content

List of Abbreviations

JCNS	Jülich Centre for Neutron Science
MCE	Magnetocaloric effect
CFCs	Chlorofluorocarbons
HCFCs	Hydrochlorofluorocarbons
HFCs	Hydrofluorocarbons
H	Magnetic field
$S(T, H)$	Total entropy
T	Temperature
$S_M(T; H)$	Magnetic entropy
$S_{lat}(T)$	Lattice entropy
$S_{el}(T)$	Electronic entropy
T_c	Curie temperature
ΔS_M	Magnetic entropy change
ΔT_{ad}	Adiabatic temperature change
M	Magnetization
C	Heat capacity
RC	refrigerant capacity
RCP	Relative cooling power
MCM	Magnetocaloric material
GMCE	Giant magnetocaloric effect
M_S	Saturation magnetization
M_r	Remanence
H_C	Coercive field
χ	Susceptibility
C	Curie constant
ϑ	Weiss constant
P	Paramagnetic
F	Ferromagnetic
AF	antiferromagnetic
T_N	Neel temperature
μ_{eff}	Effective paramagnetic moment
μ_B	Bohr magneton

f.u.	Formula unit
XRD	X-Ray Diffraction
n	Order of diffraction
λ	Wavelength
d_{hkl}	Parallel lattice planes
θ	Angle of diffraction
FWHM	Full width at half maximum
D	Particle dimension
K	Constant
R_p	Profile R-factor
y_{obs}	Observed intensity
y_{calc}	Calculated intensity
R_{wp}	Weighted profile R-factor
GOF	Goodness of fit
R_e	Expected R-factor
I_{hkl}	Total intensity
F_{hkl}	Structure factor
$f_{j,\theta}$	Atom form factor (scattering factor)
x_j, y_j, z_j	Coordinates of the atoms
R_B	Bragg R-factor
FOT	First order transition
SOT	Second order transition
ω	Detector speed
VSM	Vibrating Sample Magnetometer
PPMS	Physical Property Measurement System
ICP	Coupled Plasma-Optical
OES	Emission Spectrometry
FC	Field cooling
FW	Field warming

Chapter One   Introduction

1.1 Motivation

The magnetocaloric effect (MCE) is a magneto-thermodynamic phenomenon manifested by an adiabatic change of a material's temperature caused by exposing this material to an external magnetic field. Apart from the temperature change, the MCE can also be characterized by the isothermal magnetic entropy change **[Levitin *et al*., 1997; Gschneidner Jr. and Pecharsky, 1999; Pecharsky and Gschneidner Jr., 1999[(1)]; Pecharsky and Gschneidner Jr., 1999[(2)]; Singal *et al*., 2016].**

The MCE forms the basis for magnetic refrigeration technologies, which have developed rapidly from basic ideas to several prototype devices **[Khovaylo *et al*., 2014].** These so-called magnetic refrigerators have a series of advantages compared to conventional vapour compression refrigerators. In difference to traditional refrigerators, magnetic refrigerators do not use ozone-depleting chemicals such as chlorofluorocarbons (CFCs) and hydrochlorofluorocarbons (HCFCs), hazardous chemicals such as ammonia or greenhouse gases like hydrofluorocarbons (HFCs) which as being used in refrigerants have raised serious environmental concerns. Consequently, magnetic refrigerators are more environmentally friendly **[Brück, 2005]**.

In addition, as about 15% of the worldwide overall energy consumption originates from refrigeration, entails for searching for more energy-efficient refrigerators. The cooling efficiency in magnetic refrigerators using gadolinium was shown to reach 60% of the theoretical limit, compared to only about 40% in the best gas-compression refrigerators. This 20% difference in relative efficiency for magnetic refrigerators results in a reduced CO_2 release **[Brück, 2005; Aprea *et al*., 2015]**.

Moreover, the utilization of magnetic solid refrigerants eliminates the use of compressors, reducing significantly the noise level **[Brück, 2005]**; magnetic refrigerators are safe and durable, as there is no leakage or contamination by the refrigerant; and magnetic refrigerators are also believed to have fewer maintenance problems **[Singal *et al*., 2016]**. Due to all these advantages, magnetic refrigerators are a promising alternative technology to the conventional gaseous refrigerators near room temperature for the future **[Chen *et al*., 2009]**.

1.2 About this Thesis

The structure of this thesis can be outlined as follows: Chapter two reviews the magnetocaloric effect cycle, history of MCE and the determination methods of the MCE. Some important magnetic properties are addressed, e.g. saturation magnetization, remanence, coercive field and susceptibility. In addition, diffraction theory is introduced which includes basics of x-ray diffraction and an introduction to the LeBail and Rietveld method to extract information about the structure of the polycrystalline samples.

Chapter three introduces the materials requirements to get the optimum MCE near room temperature. A summary of previous work on the system $Mn_{5-x}Fe_xGe_{3-y}Si_y$ is also provided. Based on this, we chose to focus on the solid solutions $(Mn_5Ge_3)_x(MnFe_4Si_3)_{1-x}$ with proportions $x = 0.2, 0.4, 0.6, 0.8$.

Chapter four presents the instrumentation used on preparing and analysing the samples, including cold crucible induction melting apparatus, the powder diffractometers and the vibrating sample magnetometer of the physical property measurement system. Chapter five describes the experiments performed.

Chapter six discusses the results for the samples in the pseudo-binary system $(Mn_5Ge_3)_x(MnFe_4Si_3)_{1-x}$ with $x = (0.2, 0.4, 0.6, 0.8)$. The structure of these compounds based on LeBail and Rietveld refinements are illustrated. Furthermore, details concerning the magnetic nature of the compounds are also briefly discussed. Chapter seven provides conclusions from this study and makes suggestions for future work.

Chapter Two   Theoretical Background

2.1 Introduction to the Magneto Caloric Effect (MCE)

Magnetocaloric materials with a Curie temperature near room temperature have attracted significant interest due to their possible application for high-efficiency refrigeration devices. The magnetocaloric effect was discovered in 1918, when Weiss and Piccard observed a reversible change of temperature in nickel in the vicinity of the Curie temperature **[Smith *et al*., 2012]**.

The physical origin of the MCE is the coupling of the magnetic sub-lattice to the applied magnetic field H, which changes the magnetic contribution to the overall entropy of the solid. Figure 2.1 shows the cycle of magnetic refrigeration. Initially randomly oriented magnetic moments are aligned by a magnetic field which leads to a reduction of the magnetic entropy.

In turn, the lattice entropy increases in order to compensate the magnetic entropy reduction, resulting in heating up of the magnetic material. This heat is then removed from the material by a heat transfer medium. Removing the magnetic field at this point leads to a randomization of the magnetic moments and subsequently to an increase in the magnetic entropy. In response to this, the lattice entropy decreases again in order to compensate the magnetic entropy change, leading to a cooling of the material below ambient temperature. The difference between this temperature and the initial temperature of the material can be used for cooling **[Brück, 2005; Franco *et al*., 2012; Smith *et al*., 2012]**.
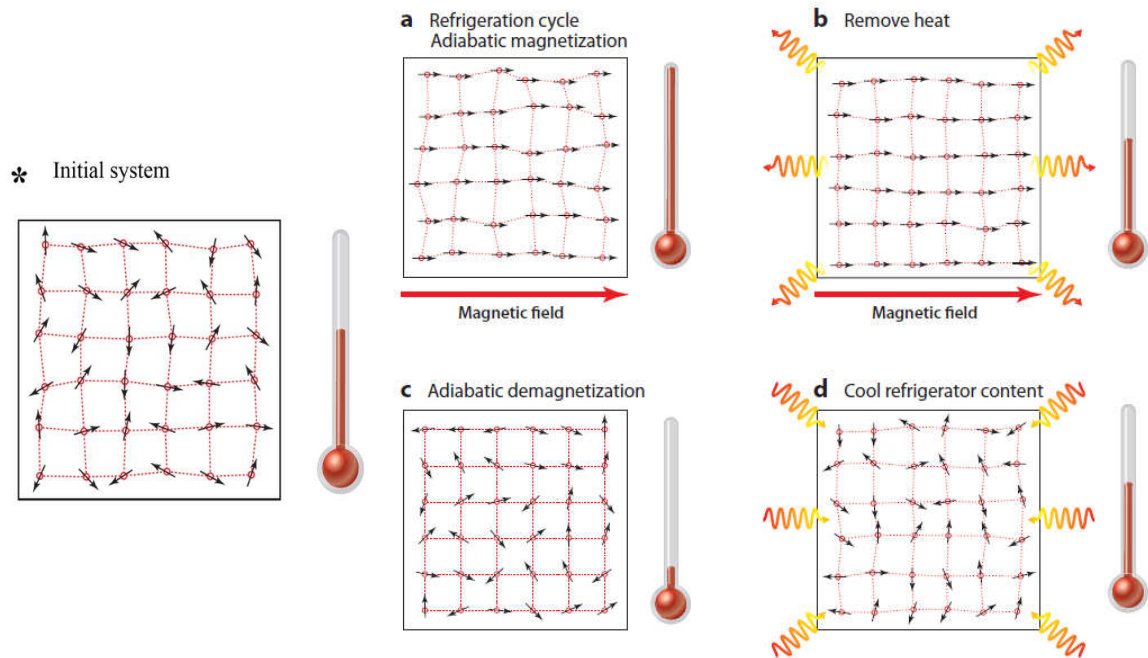
Figure 2.1: Scheme of the magnetic refrigeration cycle: (*) Initial system, (*a*) adiabatic magnetization, (*b*) remove heat, (*c*) adiabatic demagnetization, and (*d*) cool refrigerator contents **[Franco *et al*., 2012]**.

The value of total entropy $S(T, H)$ at constant pressure depends on both magnetic field strength H, and temperature T. Contributions to the overall entropy are the magnetic entropy $S_M(T, H)$ and the non-magnetic entropy (mainly lattice entropy $S_{lat}(T)$ and electronic entropy $S_{el}(T)$),

$$S(T,H) = S_M(T,H) + S_{lat}(T) + S_{el}(T) \tag{2.1}$$

Among the three, the magnetic entropy strongly depends on the magnetic field H, while usually the electronic and the lattice entropies are to a large degree magnetic-field independent.

Figure 2.2 shows a diagram of the entropy of a ferromagnet near its Curie temperature, T_c, as a function of T. The total entropy is displayed for an applied external field, H_1, and for zero field, H_0, the magnetic part of the entropy for each case (H_1 and H_0) and the thermal entropy are also shown. Applying the magnetic field adiabatically in a reversible process leads to a decrease in the magnetic entropy. To compensate this decrease and to maintain the total entropy constant, the lattice entropy is increased, $S(T_0; H_0) = S(T_1; H_1)$; as a consequence, the temperature increases: $\Delta T_{ad} = T_1 - T_0$ [**Pecharsky and Gschneidner Jr., 1999**[(3)]].
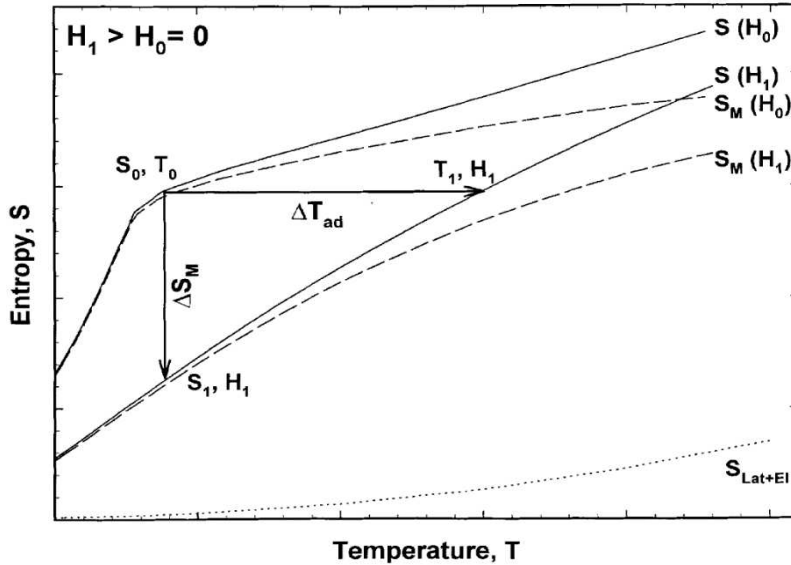
Figure 2.2: The Entropy-Temperature diagram for the MCE [**Pecharsky and Gschneidner Jr., 1999**].

When the magnetic field is applied isothermally (T remains constant), the total entropy decreases due to the decrease in the magnetic contribution, and therefore the magnetic entropy change in the process is defined as: $\Delta S_M = S(T_0, H_0) - S(T_0, H_1)$. The adiabatic temperature change ΔT_{ad} (equation 2.2) and the magnetic entropy change ΔS_M (equation 2.3) represent the two quantitative characteristics of the magnetocaloric effect. The following equations describe these two quantities and have a fundamental importance for the understanding of the

4

behaviour of the MCE in solids. They thus serve as a guide for the search of new materials with a large magnetocaloric effect [Pecharsky and Gschneidner Jr., 1999[(3)], Gschneidner Jr. *et al.*, 2005]:

$$\Delta T_{ad}(T, \Delta H) = -\int_{H_1}^{H_2} \left(\frac{T}{C(T,H)}\right)_H \left(\frac{\partial M(T,H)}{\partial T}\right)_H dH \qquad (2.2)$$

$$\Delta S_M(T, \Delta H) = \int_{H_1}^{H_2} \left(\frac{\partial M(T,H)}{\partial T}\right)_H dH \qquad (2.3)$$

With ΔH = magnetic field change, ΔT_{ad} = adiabatic temperature change, M = magnetization, C = heat capacity. Although ΔT_{ad} forms the most intuitive magnitude for characterization of the MCE, usually the value for ΔS_M is reported, as it is easier to measure [Franco *et al.*, 2012].

In addition to these two characteristic quantities, the refrigerant capacity (RC) (sometimes referred to as relative cooling power (RCP)) also represents a characteristic measure for the evaluation of the performance of a magnetocaloric material. The RC represents the amount of heat transferred between the hot and cold reservoirs (see equation 2.4) [Franco *et al.*, 2012] according to:

$$RC(H) = \int_{T_{cold}}^{T_{hot}} \Delta S_M(T, H) \, dT \qquad (2.4)$$

where T_{cold} and T_{hot} are the temperatures of the respective reservoirs.

History of the MCE
The fundamental principle of MCE was suggested independently by Debye in 1926 and Giauque in 1927. They also proposed an improved technique of cooling to very low temperatures making use of adiabatic demagnetization [Debye, 1926; Giauque, 1927]. The magnetic refrigerator was first demonstrated experimentally in 1933 by Giauque and his colleague MacDougall [Giauque and MacDougall, 1933].

Between 1933 and 1976, a number of advances in the utilization of the MCE for magnetic refrigeration were reported, most of them concerned with the refrigeration below 20 K. The idea of room-temperature magnetic refrigeration dates back to 1976 when Brown suggested and constructed a magnetic refrigerator that operated near room temperature using gadolinium as the magnetocaloric material (MCM) [Brown, 1976].

In 1997, the viability to replace vapour compression techniques with magnetic refrigeration was demonstrated. A major breakthrough was the discovery of the so-called giant

magnetocaloric effect (GMCE) in the ternary intermetallic compound $Gd_5Ge_2Si_2$. The GMCE in this compound is due to a first order ferromagnetic (I) → ferromagnetic (II) phase transition at 276 K and its unique magnetic field dependence [**Gschneidner Jr. and Pecharsky, 1999**]. In the following, many publications investigated rare earth containing compounds and several new materials classes with promising characteristics were discovered [**Smith *et al*., 2012; Gottschlich, 2013**].

2.2 Determination of Magnetocaloric Effect (MCE)

Investigations of MCE are of particular interest from two points of view, fundamental (understanding the nature of magnetic phase transitions and thermomagnetic characterization) and applied. The latter is essential to bridge material science and device engineering and focuses on promising magnetic materials and applications of the MCE for magnetic refrigeration [**Kuz'min and Tishin, 1992; Levitin *et al*., 1997; Porcari *et al*., 2013**].

There are two methods for studying the MCE, the direct measurements by monitoring the change in a material's temperature during the application/removal of the magnetic field; and the indirect one by calculating the magnetization and/or heat capacity as functions of temperature and magnetic field in the corresponding experiments [**Pecharsky and Gschneidner, Jr., 1997**].

2.2.1 Direct MCE Measurements

The direct measurement of the magnetocaloric temperature-change (which always involve measurements of the sample temperatures (initial T_0 and final T_F) in magnetic fields (initial H_0 and final H_F)) must be performed under adiabatic condition. Then the adiabatic temperature change equals to $\Delta T_{ad}(T_0, \Delta H) = T_F - T_0$ [**Pecharsky and Gschneidner Jr., 1999[(3)]; Porcari *et al*., 2013**].

One can meet the adiabatic conditions by changing the magnetic field rapidly to the extent that no considerable thermal exchange can occur. This can be achieved by keeping the sample permanently mounted and changing the magnetic field pulses rapidly ($10^{-2}\,s - 10^{-1}\,s$) by switching on and off the electromagnet; or moving the sample in and out of a constant magnetic field region slower than ($10^{-1}\,s - 10^{0}\,s$), or moving the magnet [**Dan'kov *et al*., 1997; Gopal *et al*., 1997; Pecharsky and Gschneidner Jr., 1999[(3)]; Porcari *et al*., 2013**].

Using the direct method, there are two ways to determine the temperature. The contact approach uses a sensor thermally contacted with the sample, which is best suited for a strong magnetic field and large temperature changes. The non-contact thermo-acoustic method is suited for weak magnetic fields and small temperature variations [**Glorieux *et al*., 1996; Dan'kov *et al*., 1997**], and allows rapid detection of small temperature variations induced by small periodic field variations imposed on a magnetic material [**Otowski *et al*., 1993**].

The accuracy of the direct method depends on several factors, including the quality of thermometry, the quality of the sample´s thermal insulation (a critical source of error arises when the MCE is large and disrupts the adiabatic conditions), and the quality of the compensation scheme to eliminate the effect of the changing magnetic field on the temperature sensor reading. Considering all these effects, the accuracy of the direct method lies in the 5-10 % range **[Pecharsky and Gschneidner Jr., 1999[(3)]]**.

2.2.2 Indirect MCE Measurements

There are two approaches for indirect measurements: either calculate both $\Delta T_{ad}(T, \Delta H)$ and $\Delta S_M(T, \Delta H)$ from heat capacity measurements (calorimetric method), or calculate only $\Delta S_M(T, \Delta H)$ based on magnetization measurements as a function of T and H (magnetization method). This provides $\Delta S_M(T, \Delta H)$ by numerical integration of equation 2.3, and it is useful as a rapid characterization method for the search of prospective magnetic refrigerant materials **[Foldeaki *et al*., 1995; Pecharsky and Gschneidner Jr., 1999[(3)]]**. The magnetization method is the most commonly used one **[Jeppesen *et al*., 2008]**.

It should be pointed out that, whatever the method of MCE determination is, the two characteristic measures of the MCE $|\Delta T_{ad}(T)_{\Delta H}|$ or $|\Delta S_M(T)_{\Delta H}|$ are correlated, but not equivalent, and it is not straightforward to calculate one from the other **[Pecharsky and Gschneidner, 1999[(1)]; Smith, 2012]**.

2.3 Important Magnetic Properties

One of the properties that give an indication of the nature of the magnetic material is the saturation magnetization M_S. It is the maximum of the magnetization that can be reached by application of a field. M_S represents a condition where all the magnetic moments within the material are aligned. At the saturation point, the magnetization cannot be increased further by an increase of the field (see Figure 2.3). Another magnetic property is the remanence M_r. When the applied field is removed then the material does not fully return from saturation to an un-magnetized configuration. This remaining magnetization is called the remanent magnetization **[Ashcroft and Mermin, 1976; Jiles, 1991; Blundell, 2001]**.

In order to restore the un-magnetized configuration, the application of a field in the opposite direction is necessary. The needed field is known as the coercive field H_C. The value of the coercive field depends on the type of the magnetic material. Soft magnetic materials are easy to magnetize. Thus, the magnetization is easily reversible many times. This leads to small coercive fields. Hard magnetic materials are difficult to magnetize and thus also difficult to demagnetize. Hard magnets have large hysteresis **[Ashcroft and Mermin, 1976; Jiles, 1991; Blundell, 2001]**.
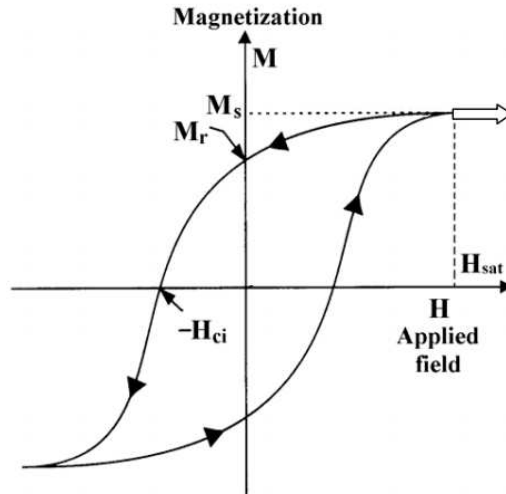
Figure 2.3: Hysteresis curve of a ferromagnetic material [**Rudowicz and Sung, 2003**].

When the material has a non-vanishing magnetic moment in the absence of a magnetic field then the material shows spontaneous magnetization. The spontaneous magnetization decreases with increasing temperature, and vanishes above a certain critical temperature. The critical temperature in ferromagnets (or ferrimagnets) is called Curie temperature and it is called Neel temperature in antiferromagnets [**Ashcroft and Mermin, 1976**].

In many paramagnets, the susceptibility χ is inversely proportional to temperature. This dependence is known as Curie's law (equation 2.5). This relation was discovered experimentally by Pierre Curie. It was later shown that Curie´s law is only a special case of a more general law, called the Curie-Weiss law (equation 2.6) [**Jiles, 1991; Cullity and Graham, 2009**].

$$\chi = C/T \tag{2.5}$$

$$\chi = C/(T - \vartheta) \tag{2.6}$$

where C is the Curie constant and ϑ is the Weiss constant with the dimensions of temperature. ϑ equals to zero for those substances which obey Curie's law. For materials that undergo a paramagnetic (P) to ferromagnetic (F) transition $\vartheta > 0$ corresponds to the Curie temperature. For materials that undergo a paramagnetic to antiferromagnetic (AF) transition the term ϑ is less than zero, although in practice the transition temperature between the paramagnetic and antiferromagnetic phases occurs at a positive temperature T_N known as the Neel temperature [**Jiles, 1991**].

If we plot $1/\chi$ versus T for a paramagnet, a straight line will result; this line will either pass through the origin (Curie behavior) or intercept the temperature axis at $T = \vartheta$ (Curie-Weiss behaviour) [**Cullity and Graham, 2009**]. The susceptibility measurements allow one to

8

calculate the effective paramagnetic moment μ_{eff} using equation 2.7 which gives μ_{eff} in SI units measured in Bohr magneton per formula unit μ_B [**Blundell, 2001**] on the basis of the mentioned plot to extract χ_M.

$$\mu_{eff} = 797.8 \, (\chi_M T)^{1/2} \tag{2.7}$$

2.4 Diffraction Theory and Structural Determination

One of the main requirements to understand the properties of a substance is to know the underlying crystal structure. In order to investigate the crystal structure of a material, scattering techniques are used which are in general non-destructive. They allow obtaining detailed insight on a crystal structure on a microscopic level. In this thesis, diffraction experiments where performed. In diffraction experiments, interference phenomena resulting from coherent elastic scattering (energy is conserved) from the crystalline structures is detected [**Cullity, 1978; Brückel *et al.*, 2018**].

2.4.1 Basics of X-Ray Diffraction (XRD)

Diffraction occurs if certain conditions are fulfilled which are described by Bragg's law. This gives the relationship between the order of diffraction (n), the wavelength (λ), the spacing of a set of parallel lattice planes (d_{hkl}), and the angle of diffraction (θ).

$$n \, \lambda = 2d \, \sin \theta \tag{2.8}$$

Figure 2.4 shows an illustration. If the path difference between two beams, which are diffracted by two parallel lattice planes is a multiple of the incident wavelength of the incoming beam then constructive interference between the wave fronts occurs. The resulting diffraction pattern of a single crystal consists of a three-dimensional distribution of reflections with specific intensities at particular positions. The positions and intensities of the reflections contain information about the crystalline structure of the material [**Sochi, 2010**].
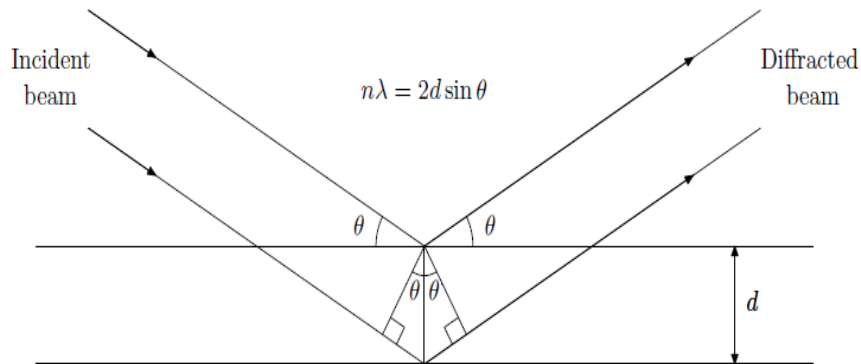
Figure 2.4: Schematic illustration of Bragg's Law [**Sochi, 2010**].

Different diffraction methods (Table 2.1) depending on the nature of the sample (single crystal, powder) and the incoming wave (mono-or polychromatic) are used in diffraction experiments.

Table 2.1: Types of diffraction techniques based on the types of radiation and the nature of the crystalline sample **[Sochi, 2010]**.

	Monochromatic X- Ray	Polychromatic Radiation
Single Crystal	Bragg	Laue
Powder	Angle Dispersive	Energy Dispersive

Within this study angle dispersive X-ray powder-diffraction experiments were performed. The basic principles are briefly explained in the following.

2.4.2 X-Ray Powder Diffraction

A polycrystalline sample consists of a large collection of very small crystallites, randomly oriented in all directions. In an ideal sample, all orientations of the crystallites exist in equal proportions. In the case of powder diffraction experiments, the types of radiation in use are X-rays and neutrons, where the wavelength is comparable to the interatomic distances in the crystal structure **[Krawitz, 2001; Ladd and Palmer, 2013; Brückel *et al*., 2018]**.

Powder diffraction has many applications across the scientific and technological spectrum, amongst others probing the state of crystalline materials and crystal structure determination. Moreover, powder diffraction is used for quantitative phase analysis and to monitor phase transformations in solids in response to pressure, temperature, stress, electric or magnetic fields, and so forth **[Sochi, 2010]**.

LeBail Method and Diffraction Diagram

The LeBail Method is an iterative least squares method **[Le Bail *et al*., 1988]**. It fits a calculated powder diffraction pattern to a measured one. The LeBail method gives access to the unit cell parameters of a crystalline compound and gives preliminary information about its space group.

In order to match the calculated powder diffraction diagram to the measured one, apart from the unit cell parameters, the background, the zero shift, and parameters describing the profile function are fitted. For the LeBail method, initial unit cell parameters of the crystalline phases must be provided as these parameters are the basis of the fitting technique. The chosen unit cell parameters should be as close as possible to the expected real values.

After calculating the diffraction diagram of the model, the difference between the calculated and observed pattern is minimized at each point of the diagram by adjusting the mentioned parameters based on the least squares method. After applying changes to the refinement parameters, to improve the agreement between calculated and observed model, a new model

diagram is calculated. These steps are repeated until a satisfactory agreement between the calculated model and observed values is reached.

The measured powder pattern is a result of the convolution of several contributions: (i) instrumental parameters and (ii) parameters related to the sample e.g. the crystal structure, structural defects, sample size and the crystallinity of the sample.

The peak shape in powder diffraction patterns can usually be described by a Voigt function which is a convolution product of Gaussian and Lorentzian functions. However, the Voigt function is in practice difficult to handle and therefore pseudo-Voigt function are often used which are linear combination of Gaussian and Lorentzian functions. Figure 2.5 shows the difference between these functions **[Guinebretiere, 2007]**.

There are significant differences in the shape of the two functions, in particular at the base: the Lorentz function has long tails on each side of the main maximum while the tails in the Gaussian function are comparatively short. The Pseudo-Voigt has intermediate properties. In general, the Gaussian contributions are predominant at low diffraction angles while the Lorentzian contributions are predominant at high angles. Thus, the peak shape depends on the diffraction angle **[Pecharsky and Zavalij, 2005; Guinebretiere, 2007]**. For certain experimental setups, it is sufficient to use simple Gaussian or Lorentzian profile functions.
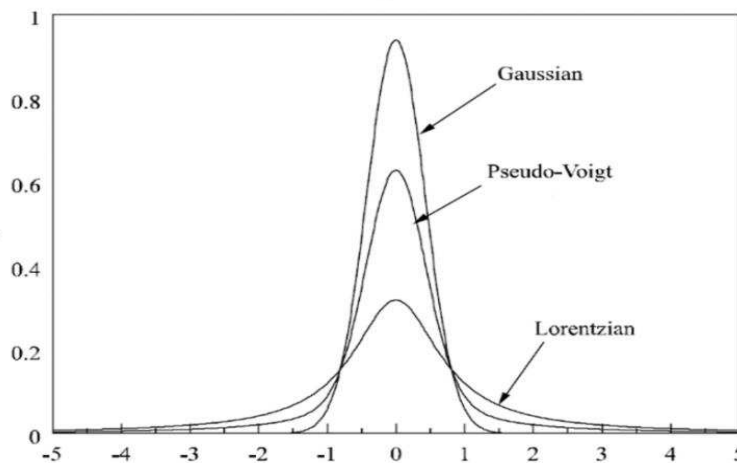
Figure 2.5: Gaussian, Lorentzian and pseudo-Voigt functions **[Guinebretiere, 2007]**.

The width of the diffraction peaks is an important parameter and directly determined by the various elements of the diffractometer. For example, the width of the diffracted peak depends on the presence of slits, which may cause the diffraction peaks to widen, and in particular their tails to spread out. The influence of the slits essentially depends on the respective sizes of the angular openings with respect to the size of the beam. If the slit's opening is about the same size as the beam, its influence on the peak profile will be small **[Krawitz, 2001;**

Guinebretiere, 2007]. The instrumental resolution also has an effect on the width of the observed peaks: the better the instrumental resolution, the narrower the peak.

The Gaussian distribution represents the effect of the instrumental broadening on the peak width. The evolution of the peak width with the Bragg angle is characteristic of the device used in the measurement. The dependence of the peak width on the Bragg angle 2θ is mostly simulated after **Cagliotti *et al*. [1958]** by the following expression for the Gaussian FWHM: **[Will, 2006; Guinebretiere, 2007; Dinnebier and Billinge, 2008]**.

$$\text{FWHM} = \text{U} \tan^2 \theta + \text{V} \tan \theta + W \tag{2.9}$$

where *U*, *V* and *W* are adjustable (fit) parameters. The initial and approximate starting values can be found prior to the experiment by measuring the full width at half maximum, FWHM, in a standard sample. These values remain basically unchanged as long as the experimental setup is kept **[Krawitz, 2001; Will, 2006; Guinebretiere, 2007]**.

Two additional parameters affect the FWHM. These two parameters are X and Y, which are related to the Lorentzian distribution, and which represent the effect of specimen broadening on the peak width. X and Y are coefficients of $1/\cos\theta$ and $\tan\theta$. They both together provide a complete description of the Lorentzian FWHM **[Pecharsky and Zavalij, 2005]**. The width of the peaks is directly related to the size of the coherently scattering regions. Thus, there is a direct effect of the dimension of the particle on the FWHM which is represented by Scherrer's equation **[Krawitz, 2001]**.

$$W_{\text{FWHM}} = \frac{K\lambda}{D \cos \theta} \tag{2.10}$$

where *D* is the particle dimension, *K* is a constant.

In addition to the peak shape, the accurate determination of the diffraction angle of the peaks is of particular importance when describing the diffraction pattern. Thus, the important shift parameter must be considered. It is constant over the whole range of Bragg angles, and describes an offset of the zero point of the Bragg angles. This is due to a shift in setting zero position for one or more diffractometer axes (detector and/ or X-ray source). The zero-shift could arise from inaccurate centring of the sample or sample holder. The effect is largest for small diffraction angles and decreases for higher diffraction angles **[Krawitz, 2001; Pecharsky and Zavalij, 2005]**.

Powder patterns always contain statistical noise or scattering contributions that do not originate from diffraction of the sample. The main contributions to the background are elastic scattering from the sample holder, an amorphous part of the sample, or from air in the beam-

path, fluorescence radiation and scattering from the used foil. Due to the construction of slits in front of the X-ray tube, the background decreases (more or less) with increasing 2θ. **[David *et al.*, 2002; Dinnebier and Billinge, 2008]**. In the LeBail refinement the contribution from the background has to be properly taken into account.

The quality of the fit of the calculated pattern with respect to the observed pattern is judged by means of numerical criteria. Denoting $y_{obs,j}, y_{calc,j}$ as the observed, and calculated intensities of the specific diffraction profile points, the most common useful criteria are**:**

$$R_p = \frac{\sum_j |y_{obs,j} - y_{calc,j}|}{\sum_j y_{obs,j}} \tag{2.11}$$

which is called the profile R-factor, and

$$R_{wp} = \sqrt{\frac{\sum_j w_j (y_{obs,j} - y_{calc,j})^2}{\sum_j w_j y_{obs,j}^2}} \tag{2.12}$$

which is the weighted profile R-factor. R_{wp} is optimized using the least squares method, and indicates the overall refinement quality. w_j is a weighting factor $w_j = 1/y_{obs}$. Another criterion is the Goodness Of Fit (χ^2 or GOF):

$$\chi^2 = \left(R_{wp} / R_e \right)^2 \tag{2.13}$$

Where R_e is the statistically expected R-factor:

$$R_e = \frac{N - P + C}{\sum_j w_j (y_{obs,j})^2} \tag{2.14}$$

N is the number of observations (points measured) in the experimental powder profile, P is the number of parameters refined, and C is the number of constraints. In general, N is much greater than (P + C) so that the numerator is generally close to the value of N **[Pecharsky and Zavalij, 2005; Ladd and Palmer, 2013]**. χ^2 reflects the influence of adding new variables to the refinement process, and shows whether introducing new variables can lower the error **[Guinebretiere, 2007]**.

Rietveld Method

The Rietveld refinement is curve fitting based on a least squares method to obtain the best fit between an the experimental and the corresponding calculated powder diffraction patterns. A reliable refinement can be useful only when the number of observations highly exceeds the number of parameters used **[Rietveld, 1967; David *et al.*, 2002; Ladd and Palmer, 2013]**.

While the LeBail method provides information about the lattice parameters, and an idea about the space group (which can be deduced and refined from the peak positions and systematically absent reflections), the Rietveld method confirms the space group type and additionally provides information about, for example, the atom coordinates in the unit cell, strain, atomic displacement parameters, etc.

Originally, the Rietveld method can be applied only when an initial structural model is available. However, **LeBail *et al.* [1988]** reported that the Rietveld approach could be extended to cases with no initial structural model, by applying the least squares method to deduce some initial lattice parameters. Hence, the LeBail method is a first step in solving the crystal structure from powder diffraction data **[David *et al.*, 2002; Ladd and Palmer, 2013]**.

The Rietveld method is based on considering the complete powder diffraction pattern using a variety of refinable parameters. Therefore, it is called a full pattern or full profile refinement. In addition to the parameters that are refined in the LeBail method, additional parameters can also be adjusted (i.e. atomic positions (x, y, z), atomic site occupancies, atomic displacement parameters**,** preferred orientation, phase volume fractions, etc. **[David *et al.*, 2002; Pecharsky and Zavalig, 2005; Will, 2006]**.

In the case of the LeBail method, the atomic positions in the unit cell are not considered, only the cell parameters and the space group are determined. As a result, no structure factors can be calculated and it is assumed that all the integrated intensities are initially equal. In the Rietveld method, the atoms positions in the unit cell are considered and it is thus possible to calculate integrated intensities **[David *et al.*, 2002; Will, 2006; Guinebretiere, 2007]**. The total intensity (equation 2.15) is proportional to the square of the structure factor:

$$I_{hkl} \sim |F_{hkl}|^2 \tag{2.15}$$

The structure factor (equation 2.16), F_{hkl} is defined as:

$$F(hkl) = \sum_{j=1}^{n} f_{j,\theta} \, exp\big[i2\pi\big(hx_j + ky_j + lz_j\big)\big] \tag{2.16}$$

where $f_{j,\theta}$ is the atom form factor (scattering factor) of atom j and x_j, y_j, z_j are the coordinates of the atoms j in the unit cell.

To begin the fitting procedure in a Rietveld refinement, follow an iteration procedure. A zero model for cell parameters, space group, and atomic positions in the unit cell is provided **[Will, 2006]**. This model values are refined by the least squares method; to be used as starting values for the next iteration. The process continues until some limiting improvement is reached **[McCusker, *et al.*, 1999]**. To assess the quality of the model, the Bragg R-factor as well as R_F are used in addition to the agreement factors used in the LeBail refinement:

Bragg R-factor:

$$R_B = \frac{\sum_{hkl}|I_{hkl}(obs) - I_{hkl}(calc)|}{\sum_{hkl}|I_{hkl}(obs)|} \tag{2.17}$$

and R_F:

$$R_F = \frac{\sum_{hkl}|F_{hkl}(obs) - F_{hkl}(calc)|}{\sum_{hkl}|F_{hkl}(obs)|} \tag{2.18}$$

which gives an indication of the agreement between the observed and the calculated structure factors.

Chapter Three   Previous Work

3.1 Materials Requirements

Over the past 10 years, in the research for optimum magnetic refrigeration efficiency near room temperature, the magnetic and magnetocaloric properties of different compound families were investigated. In general, significant magneto-thermal effects are the basic selection criteria for these materials. In addition, the choice of suitable materials depends on several factors like properties, performance, environmental acceptability, and economics.

All magnetic substances exhibit the MCE **[Pecharsky and Gschneidner Jr., 1999[(3)]; Smith et al., 2012]**. However, one of the main features for choosing the ideal compound is that it undergoes a magnetic phase transition, as the magnetocaloric effect at these critical points manifests maximum values **[Singal et al., 2016]**.

In order to obtain excellent refrigeration efficiencies, a considerable refrigerant capacity (RC) is essential, besides the large entropy change. Many materials undergo a first order magnetic phase transition (FOT), where usually the change in magnetic entropy is large. However, the transitions are often accompanied by discontinuous structural changes or unit cell volume variations. In addition, these materials exhibit large hysteresis. These effects lead to a fatigue of the materials which greatly weakens the MCE and the RC after several refrigerant cycles. Due to this, the practical applications are limited **[Zhao et al., 2006; Chen et al., 2009; Halder et al., 2011; Zheng et al., 2012]**.

Hence, it is necessary to explore magnetic materials with a large reversible MCE at low applied fields and good RC based on a phase transition with second order characteristics. Materials with a second order transition (SOT) have reduced magnetic and thermal hysteresis and thus an enhanced refrigerant capacity and they are not subject to the various drawbacks associated with FOT **[Chen et al., 2009; Halder et al., 2011; Zheng et al., 2012; Brock et al., 2017; Chaudhary et al., 2019]**.

Additional selection criteria include suitable physical and engineering properties important for manufacturability and operation of the refrigeration machine e.g. to have large saturation magnetization and good chemical stability and to be easy for processing **[Chaudhary et al., 2019]**. These will be reasonably applied only to materials which showed a significant magnetocaloric effects **[Földeàki et al., 1995]**.

For the studies which aim at the elucidation of the fundamental mechanism of the MCE, it is furthermore important that these materials can be synthesized as large single crystals, as this opens a wide range of experimental methodologies **[Qiu, 2014]**.

3.2 The System $Mn_{5-x}Fe_xGe_{3-y}Si_y$

In the following, a short overview of literature in relation to compounds in the system $Mn_{5-x}Fe_xGe_{3-y}Si_y$ on which this study is focused will be provided.

The binary compound Mn_5Si_3 crystallizes hexagonal in space group *P6₃/mcm* with lattice parameters $a = 6.916$ Å and $c = 4.824$ Å ($c/a = 0.698$) according to **Kappel *et al*. [1976]** and $a = 6.910$ Å and $c = 4.814$ Å ($c/a = 0.697$), according to **Ramos *et al.* [2002]**. The structure belongs to the $D8_8$, structure type. The antiferromagnetic structure of Mn_5Si_3 was investigated by neutron diffraction at low temperatures **[Lander *et al*., 1967]**. **Vinokurova *et al*. [1995]** showed on the basis of *ac*-susceptibility and magnetization measurements that Mn_5Si_3 single crystal exhibits first order transitions. The two first order magnetic transitions were at 66 K between two antiferromagnetic phases (AF1 and AF2) and at 99 K from antiferromagnetic to paramagnetic phase **[Menshikov *et al*., 1990]**.

The bulk and nanostructure of the binary compound Fe_5Si_3 was investigated by **Skomski *et al*. [2018]**. They found that the bulk intermetallic crystallizes in the Mn_5Si_3-type hexagonal structure. The samples, produced by rapid quenching (bulk) and cluster deposition (nanoparticulate thin films), have Curie temperatures of about 400 K. The lattice constants of the bulk Fe_5Si_3 are a = 6.722 Å and c = 4.680 Å. The material is close to the onset of ferromagnetism.

The Fe-Ge system forms one of the richest binary intermetallic systems both in terms of the number of intermediate phases and diversity of crystal structures and magnetic properties. The diversity of physical properties, mainly thermodynamic property, is associated with the diversity of the crystal structures of compounds in the Fe-Ge system. The magnetic phases of the Fe-Ge system are varying from ferromagnets to antiferromagnets with complex magnetic structures **[Khalaniya and Shevelkov, 2019]**.

The binary intermetallic compound Mn_5Ge_3 is of particular interest due to the fact that it is a ferromagnetic material with a Curie temperature close to room temperature. Several powder and single crystal diffraction experiments have been performed on this compound (Table 3.1). In addition, a study of nanoparticles is also provided. The compound is isotypical to Mn_5Si_3. However, in contrast to Mn_5Si_3, Mn_5Ge_3 is a strong ferromagnet **[Ohoyama, 1961; Liu and Altounian, 2006]**. It undergoes a second-order phase transition (SOT) which gives rise to a large magnetocaloric effect in the vicinity of its Curie temperature due to the rapid change of the magnetization **[Songlin *et al*., 2002[(1)]]**. Table 3.1 summarizes the Curie temperatures and the lattice parameters of Mn_5Ge_3 obtained by several research groups. The methods used for the investigation of the properties are also included in Table 3.1. Lattice parameters determined for Mn_5Ge_3 by different groups are in good agreement.

In spite of the fact that Mn_5Ge_3 undergoes a second-order phase transition with the MCE of suitable characteristics, the use of this high content of germanium limits its use on a large

scale. So many researchers replace Ge partially with other elements like Sb, Al, Ga and Si [**Sun *et al*., 2017**].

Table 3.1: Curie temperatures and lattice parameters for Mn_5Ge_3 according to the literature.

synthesized material		Lattice parameters (Å)	*c/a*	Used method	T_c (K)	Reference	
						Reference for T_c	Main reference
Powder		a = 7.184 c = 5.053	0.703		320	[Castelliz,1955]	[Ciszewski, 1963]
					304	[Kanematsu, 1962]	
					293	[Fontaine and Pautrenet, 1962]	
					300	[Brayinski and Ciszewski, 1963]	
					300	[Wreciono, 1963]	
Single				Magnetization measurements	304	[Yasukochi *et al*.]	[Tawara and Sato, 1963]
Powder		a = 7.195 c = 5.032	0.699		296		[Kappel *et al*., 1976]
Single		a = 7.184(2) c = 5.053(2)	0.7030(3)		304	[Tawara and Sato, 1963]	[Forsyth and Brown, 1990]
Powder					298		[Songlin *et al*., 2002[(1)]]
Powder		a = 7.204(2) c = 5.028(2)	0.6980(3)	ac-susceptibility, dc-magnetization measurements	298		[Liu and Altounian, 2006]
Powder				Magnetization measurements	296		[Zhang *et al*., 2007]
Powder		a = 7.197 c = 5.036	0.700	Magnetization measurements	296		[Zheng *et al*., 2012]
Powder		a = 7.197 c = 5.036	0.700	Heat capacity, magnetization measurements	297.4(2)		[Tolinski and Synoradzki, 2014]
Powder		a = 7.20 c = 5.05	0.701	Magnetization measurements	290		[Kim *et al*., 2015]
Powder		a = 7.2050 c = 5.0351	0.699		295		[Carroll *et al*., 2017]
Nanoparticles	Average size (nm)			Magnetization measurements			[Tosun *et al*., 2018]
	7.2	a = 7.183 c = 5.080	0.707				
	10	a = 7.167 c = 5.011	0.699				
	12.6	a = 7.193 c = 5.078	0.706				

Based on the consideration of the magnetic interactions of the two compounds Mn_5Si_3 and Mn_5Ge_3 one might conclude that the incorporation of the smaller Si leads to a strengthening of the antiferromagnetic interactions. Indeed, **Kappel *et al*. [1976]** who investigated the system $Mn_5Ge_{3-y}Si_y$, with $3 \geq y \geq 0$ claim that as the Si concentration increases, the antiferromagnetic interactions also increase.

Curie temperatures determined by Kappel *et al*. for the concentration range $0 \leq y \leq 2.25$ show a decrease of T_c with increasing Si-content. However, all compounds in this concentration range exhibit ferromagnetic ordering (Table 3.2). Also, magnetization

measurements in fields of up to 33 kOe at 4.2 K confirm a ferromagnetic character of the magnetic ordering for these Si contents. At values of $y > 2.4$ the compounds are characterized by increasing antiferromagnetic interactions. Finally, these become predominant at about $y = 2.85$. As a consequence of the incorporation of the smaller Si, lattice parameters (Table 3.3) also decrease with increasing Si content. However, the ratio c/a remains invariant for all compositions. According to the authors the average magnetic moment decreases due to the volume effect from 2.6 μ_B for $y = 0$ to 2.15 μ_B for $y = 2.25$ [Kappel *et al.*, 1976].

Table 3.2: Curie temperature for $Mn_5Ge_{3-y}Si_y$ in the range $0 \le y \le 3$ [Kappel *et al.*, 1976].

y	0	0.3	0.6	0.9	1.2	1.5	1.8	2.1	2.25
T_c (K)	296	290	283	278	265	256	228	176	151

Table 3.3: Lattice parameters and c/a ratios in the system $Mn_5Ge_{3-y}Si_y$ [Kappel *et al.*, 1976].

y	0	0.3	0.6	0.9	1.2	1.5	1.8	2.1	2.25	2.4	2.7	3
a	7.195	7.183	7.153	7.123	7.076	7.071	7.027	7.010	6.998	6.977	6.925	6.916
c	5.032	5.019	4.996	4.984	4.948	4.943	4.907	4.893	4.886	4.872	4.831	4.824
c/a	0.699	0.699	0.698	0.700	0.699	0.699	0.698	0.698	0.698	0.698	0.698	0.698

The system $Mn_5Ge_{3-y}Si_y$ with $y = 0 - 1.5$ was also studied using *ac*-susceptibility and *dc*-magnetization measurements and X-ray diffraction by **Liu and Altounian [2006]**. They found a decrease of the lattice parameters from $a = 7.204(2)$ Å and $c = 5.028(2)$ Å to $a = 7.084(2)$ Å and $c = 4.945(3)$ Å with increasing Si content. All the compounds crystallize in space group $P6_3/mcm$. They show ferromagnetic ordering and their Curie temperatures T_c, decrease from 298 to 252 K as the Si content is increased.

According to the authors, ΔS_M also decreases with increasing Si content. They assumed that the nature of the magnetic ordering is very sensitive to the Mn-Mn distance in the compounds which decreases with increasing Si content. The decrease in magnetization and ΔS_M with increasing Si content is attributed to the variation of the exchange interaction induced by the reduction of Mn-Mn distances [Liu and Altounian, 2006].

Zhao *et al.* [2006] studied the same series with $y = 0.1, 0.3, 0.5, 1.0, 1.5$ and 2. They confirmed that all $Mn_5Ge_{3-y}Si_y$ compounds crystallize in the Mn_5Si_3-type hexagonal structure with space group $P6_3/mcm$ in agreement with Liu and Altounian. Their lattice parameters are in excellent agreement with the ones reported by **Kappel *et al.* [1976]** (see Figure 3.1) and they observed a decrease of the Curie temperature for larger y values, while for small values ($y < 0.5$) T_c is hardly changed (see Table 3.4). Again, also their reported Curie temperatures are in excellent agreement with the values reported by **Kappel *et al.* [1976]** (see Figure 3.2). According to them, the Si substitution has two effects: the magnetic-entropy change decreases with increasing Si content and the peak of the magnetocaloric effect becomes broadened [Zhao *et al.*, 2006].

Table 3.4: Lattice parameters and the Curie temperature of $Mn_5Ge_{3-y}Si_y$ [**Zhao** *et al*.**, 2006**].

Materials (*y*)	Lattice constants (Å)		*c/a*	Curie temperature (K)
0.1	*a* = 7.179	*c* = 5.019	0.699	300
0.3	*a* = 7.157	*c* = 5.010	0.700	300
0.5	*a* = 7.142	*c* = 4.993	0.699	299
1.0	*a* = 7.103	*c* = 4.954	0.697	283
1.5	*a* = 7.046	*c* = 4.926	0.699	258
2.0	*a* = 6.999	*c* = 4.890	0.699	198
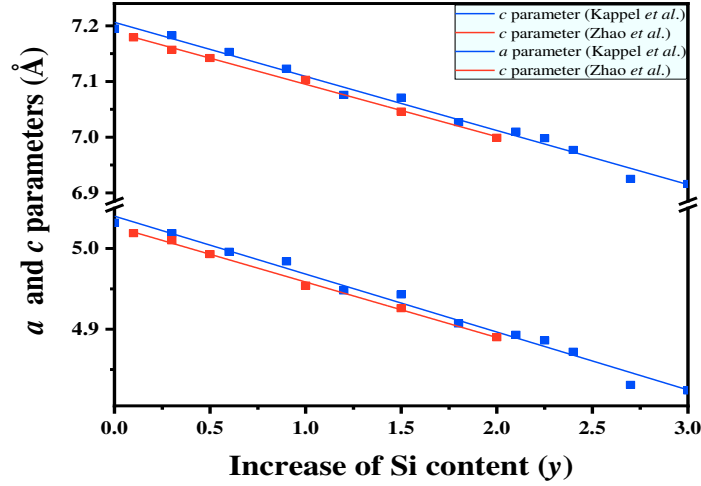
Figure 3.1: Lattice parameters of $Mn_5Ge_{3-y}Si_y$ as a function of *y*. Data from [**Kappel** *et al*.**, 1976**] and [**Zhao** *et al*.**, 2006**].
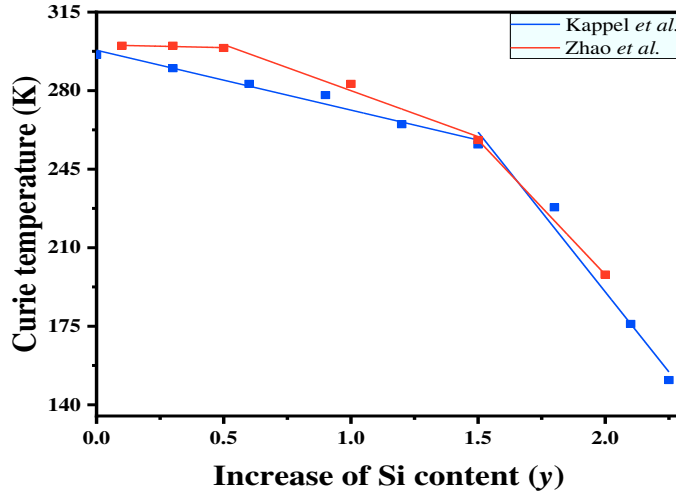
Figure 3.2: Dependence of the Curie temperature of compounds in the system $Mn_5Ge_{3-y}Si_y$ on the compositional parameter *y*. Data from [**Kappel** *et al*.**, 1976**] and [**Zhao** *et al*.**, 2006**].

In the case of the series $Mn_{5-x}Fe_xGe_3$ with $x = 0, 0.25, 0.5, 0.75$ and 1.0, which was studied by magnetization measurements, increasing Fe leads to superior material properties for applications at room-temperature magnetic refrigeration. This is due to the observed increase of magnetic entropy change and enhanced refrigeration capacity (RC) [**Zhang** *et al*.**, 2007**].

According to this study, saturation magnetization increases with Fe content reaching a maximum at $x = 0.5$, then decreases with further Fe substitution. Table 3.5 gives the reported refrigerant capacity of $Mn_{5-x}Fe_xGe_3$ compounds for fields up to of 5 T [**Zhang *et al.*, 2007**].

Table 3.5: Refrigerant capacity of $Mn_{5-x}Fe_xGe_3$ compounds for an applied field of 5 T [**Zhang *et al.*, 2007**].

Compound	RC (J Kg^{-1})
Mn_5Ge_3 ($T_c = 296°K$)	205
$Mn_{4.75}Fe_{0.25}Ge_3$	212
$Mn_{4.5}Fe_{0.5}Ge_3$	227
$Mn_{4.25}Fe_{0.75}Ge_3$	216
$Mn_4Fe_1Ge_3$	237

Brock *et al.* also studied the series $Mn_{5-x}Fe_xGe_3$ using magnetization measurements with low iron contents ($0 \leq x \leq 0.15$; step of 0.05). In agreement with **Zhang *et al.* [2007]**, they found that the maximum of the refrigerant capacity is observed for their sample with the highest Fe content (Table 3.6). For all Fe concentrations, the alloys are ferromagnetic and undergo a second-order ferromagnetic-to-paramagnetic transition near room temperature. Although the small Fe doping has little effect on the Curie temperatures of the system, changes in the saturation magnetization M_S were observed. Initially, it increases with $x = 0$ until $x = 0.05$ and then decreases with further increase of x [**Brock *et al.*, 2017**].

Table 3.6: Refrigerant capacity of $Mn_{5-x}Fe_xGe_3$ compounds for an applied field of 20 kOe and 50 kOe [**Brock *et al.*, 2017**].

Compound	RC (J kg^{-1})	
	For 20 kOe	For 50 kOe
Mn_5Ge_3	97	298
$Mn_{4.95}Fe_{0.05}Ge_3$	95	294
$Mn_{4.9}Fe_{0.1}Ge_3$	104.5	305
$Mn_{4.85}Fe_{0.15}Ge_3$	108.50	312

The magnetocaloric effect of $Mn_4FeGe_{3-y}Si_y$ compounds was studied by **Halder *et al.* [2011]** using *dc* magnetization measurements. The investigated compounds in the $Mn_4FeGe_{3-y}Si_y$ series for $y = 0, 0.2, 0.6$ and 1 are found to undergo a second-order magnetic phase transition. T_c for $y = 0$ is above room temperature (320 K) and initially remains constant for small Si substitution at the Ge site and then decreases marginally with a further increase in Si concentration (320, 320, 319 and 318 K for $y = 0, 0.2, 0.6$ and 1, respectively).

This decrease in T_c could be again closely related to the change in Mn-Mn interactions which occurs due to the reduction in the Mn-Mn distance. The saturation magnetization at 5 K remains almost constant for all samples. The change in magnetic entropy at T_c under a magnetic field variation of 50 kOe is increased when Si is replacing Ge.

Figure 3.3 shows that with increasing Si content, the value of ΔS_M decreases slower. This is because the magnetic transition spreads over a broad temperature range. Thus, by substituting Si at the Ge site, the operating temperature range increases, which is important for practical applications **[Halder *et al*., 2011]**.
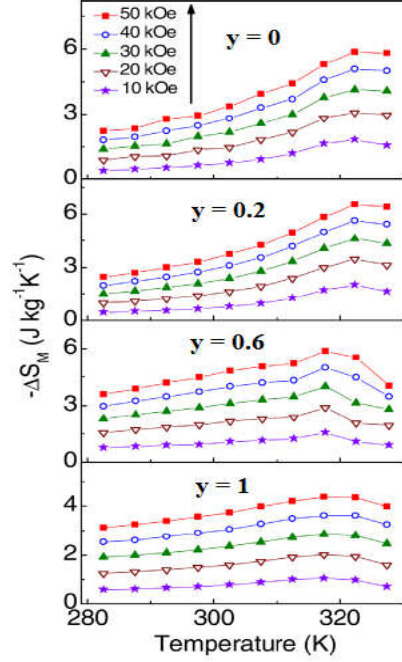
Figure 3.3: Magnetic entropy change versus temperature for y = 0, 0.2, 0.6, and 1 samples in the $Mn_4FeGe_{3-y}Si_y$ series **[Halder *et al*., 2011]**.

Another series in the quaternary system $Mn_{5-x}Fe_xGe_{3-y}Si_y$ consists of the solid solution between Mn_5Si_3 and Fe_5Si_3. $Mn_{5-x}Fe_xSi_3$ compounds are well known for their magnetocaloric properties. X-ray powder diffraction analysis showed that the compounds all crystallize with the hexagonal symmetry *P*6$_3$/*mcm* at ambient temperature **[Binczycka *et al*.,1973; Candini *et al*., 2004; Herlitschke *et al*., 2016]**. However, neutron single crystal diffraction investigations indicate that the symmetry of the crystal structure of $MnFe_4Si_3$ is reduced to *P-6* **[Hering *et al*., 2015]**. Table 3.7 shows lattice parameters for different *x* parameters **[Binczycka *et al*., 1973]**. The lattice parameters and unit cell volume become smaller with increasing iron content due to the smaller atomic radius of the Fe-atom when compared to Mn **[Johnson *et al*., 1972]**.

Table 3.7: Lattice parameters of compounds in the $Mn_{5-x}Fe_xSi_3$ system **[Binczycka *et al*., 1973]**.

x	*a*	*c*	c/a
0	6.9077(4)	4.8131(4)	0.69680(7)
1	6.8849(9)	4.7861(8)	0.6952(1)
2	6.8538(5)	4.7579(5)	0.69420(9)
3	6.8301(4)	4.7390(4)	0.69380(7)
4	6.8054(7)	4.7290(5)	0.6949(1)

The magnetic behaviour of the compounds in the system $Mn_{5-x}Fe_xSi_3$ was investigated by **Songlin** *et al.* **[2002[(2)]]**. Depending on the compositional parameter *x,* different magnetic ordering types for $Mn_{5-x}Fe_xSi_3$ compounds were identified (Figure 3.4). For Mn_5Si_3 , two antiferromagnetic (AF) structures where found at low temperature, while Fe_5Si_3 is ferromagnetic above room temperature (F).

Mn-rich compounds in the series show antiferromagnetic properties, whereas the Fe-rich compounds have ferromagnetic properties **[Binczycka *et al.*, 1973; Candini *et al.*, 2004]**. The transition temperatures to the magnetically ordered phase increase with increasing Fe-content. The largest value for the magnetic-entropy change in this series was observed for the $MnFe_4Si_3$ compound. This compound is of particular interest as the transition temperature T_c is close to room temperature.
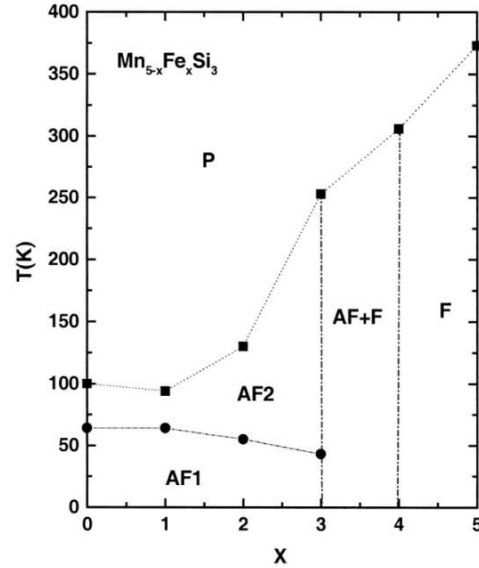
Figure 3.4: Sketch of a magnetic phase diagram for the $Mn_{5-x}Fe_xSi_3$ compounds **[Songlin *et al.*, 2002[(2)]]**.

Based on the literature results, we chose to focus on the solid solutions of Mn_5Ge_3, and $MnFe_4Si_3$ with proportions (0.2, 0.4, 0.6, 0.8). Both end members have transitions to ferromagnetic structures close to room temperature, which are accompanied by sizeable magnetocaloric effects. Compounds in this solid solution therefore form a promising class of materials. In addition, they consist mainly of abundant elements (Mn, Fe, Si) and do not contain toxic elements like As, nor expensive rare earth elements like Gd. These are major advantages when their potential for magnetocaloric refrigeration is considered.

Chapter Four   Instrumentation

4.1 Cold Crucible Induction Melting (CCIM) Apparatus

The cold crucible induction melting (CCIM) is an innovative process to melt high temperature reactive materials like Titanium, Tantalum, Niobium and Molybdenum, especially when high purity of the samples is required. The use of e.g. a copper crucible instead of a crucible out of ceramic material or graphite prevents contamination by the crucible material and provides a high purity melt [**Pericleous** *et al*.**, 2006; Mühlbauer, 2006; Quintana** *et al*.**, 2011; Windsheimer** *et al*.**, 2015**].

In addition to a high purity melt, CCIM is a fast method, comparatively easy to execute, and provides excellent thermal and chemical homogenization of the melt [**From: http://www.ald-dynatech.com**].
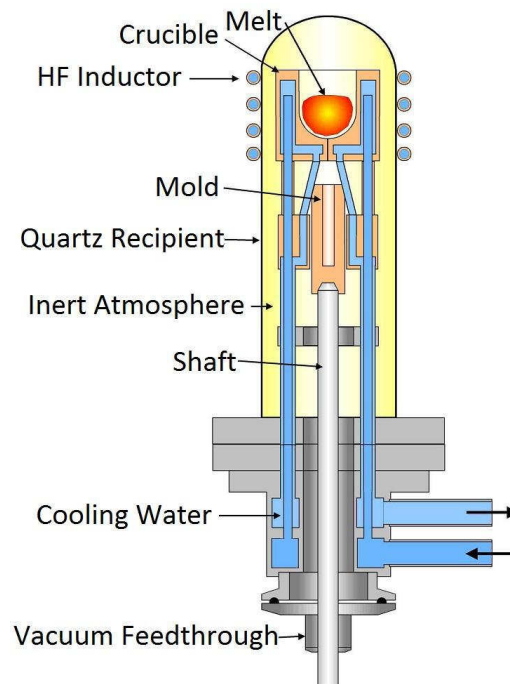
Figure 4.1: Scheme of a cold crucible induction melting apparatus [**Beyss and Gier, 2014**].

Figure 4.1 shows a scheme of the main parts of the apparatus used for CCIM. In this system, the crucible consists of several segments, which are closely spaced with respect to each other without directly touching. As seen from Figure 4.2a, these vertical segments form the walls of the crucible into which the raw material is placed [**Gombert** *et al*.**, 2002; Quintana** *et al*.**, 2011**].
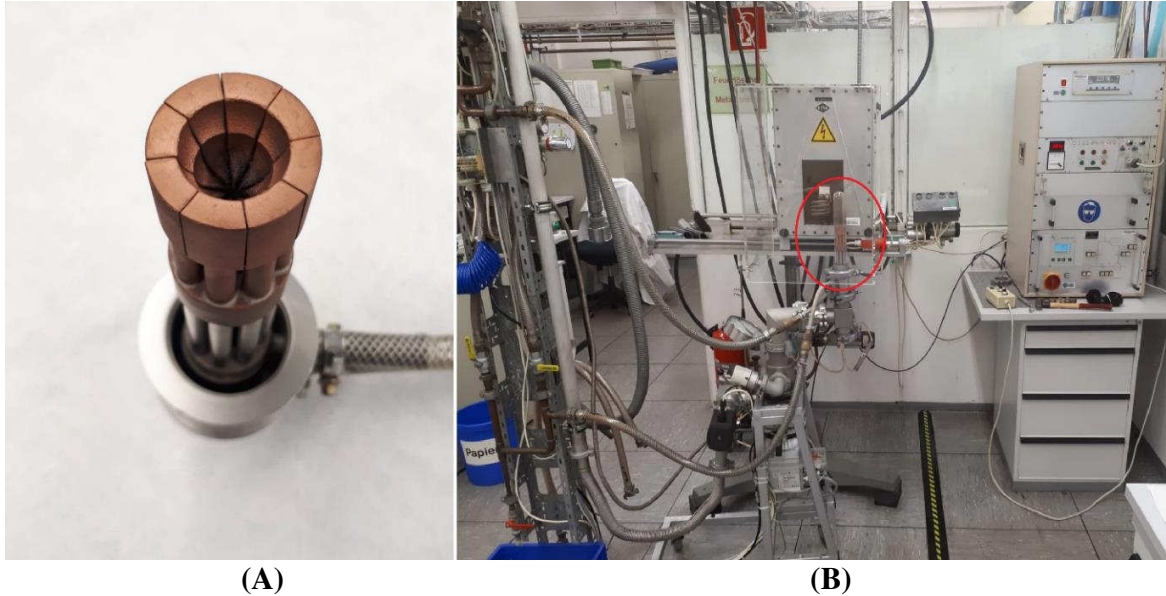
Figure 4.2: A) Photo of the used copper crucible; B) Photo of the whole CCIM apparatus.

The purpose of building up the crucible with small gaps in between is to make them electrically isolated against each other. This provides sufficient electromagnetic transparency to the induced field. Thus, the inductive field generated by the surrounding coil can pass through the crucible wall and interact with the contents of the crucible **[Gombert *et al*., 2002; Mühlbauer, 2006; Quintana *et al*., 2011].**

The necessary energy to heat the sample up is generated by an electromagnetic field induced by an induction coil surrounding the crucible. This induction coil transforms the output of the high frequency generator into a varying magnetic field. The generated field induces eddy currents in the conductive material inside the crucible. The eddy currents are dissipated by the electrical resistivity of the material causing joule-heating (also called resistive losses). This causes the material to heat up **[Gombert *et al*., 2002; Mühlbauer, 2006; Quintana *et al*., 2011; Windsheimer *et al*., 2015]**.

When the sample is molten, the AC coil causes induction leading to a levitation of the melt and pushing it away from the water-cooled surfaces **[Gombert *et al*., 2002; Pericleous *et al*., 2006; Quintana *et al*., 2011]**.

Two water-cooled circuits, one for the crucible and the other for the induction coils, are present. In addition to cooling, water in the metallic crucible prevents contamination of highly reactive melts. The system is furthermore connected to two evacuating pumps and an Argon source. For safety, the cold crucible is covered by glass (Figure 4.2b).

4.2 Powder Diffractometers

Two principal types of diffractometer geometries were used during this work. The main parts, regardless of the geometry, are an X-ray source, a monochromator, a collimator, the sample stage, and the detector.

The X-ray beam originating from the X-ray tube is composed of several wavelengths. There are two common techniques that can be used to get a monochromatic radiation; using filters or a monochromator. The filters consist of a thin sheet of a material that absorbs all of the emitted radiation with wavelengths other than the selected, while the monochromator usually consists essentially of a single crystal of e.g. quartz, silicon, or germanium, etc. In the crystal, the beam of desired wavelength is separated from the polychromatic broad band of radiation by diffraction according to Bragg's law (see Figure 4.3) **[Ladd and Palmer, 2013]**.
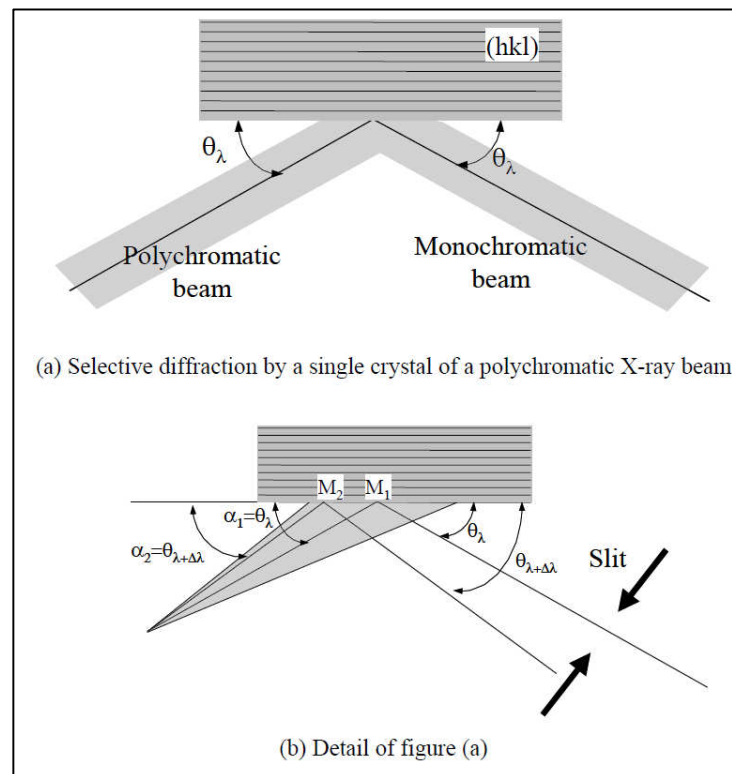
Figure 4.3: Scheme of Bragg diffraction on a monochromator crystal **[Rene Guinebretiere, 2007]**.

4.2.1 The Huber Diffractometer with G670 Guinier Camera (Transmission Geometry)

Figure 4.4 shows a schematic view of the powder diffractometer setup with Guinier geometry. The camera enclosure may be evacuated in order to decrease the background scattering **[Ladd and Palmer, 2013].**
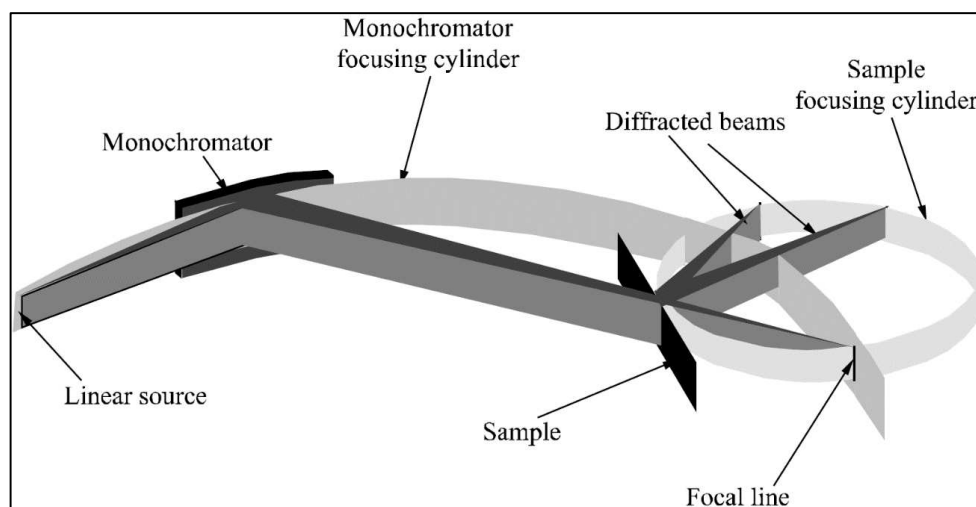
Figure 4.4: A scheme of the diffractometer setup with Guinier geometry **[Rene Guinebretiere, 2007]**.

In-house powder diffraction experiments at the JCNS-2 institute were performed using the Huber G670 Guinier camera which functions in transmission geometry (Figure 4.5a). This diffractometer uses monochromatic radiation with a wavelength of 1.541 Å ($K\alpha_1$ radiation). In order to achieve this wavelength, a suitable Germanium single crystal is placed between the source and the sample, which eliminates other characteristic emission lines and the Bremsstrahlung. This leads to a reduction of background scattering in the diffraction diagram**.**

(A)   **(B)**
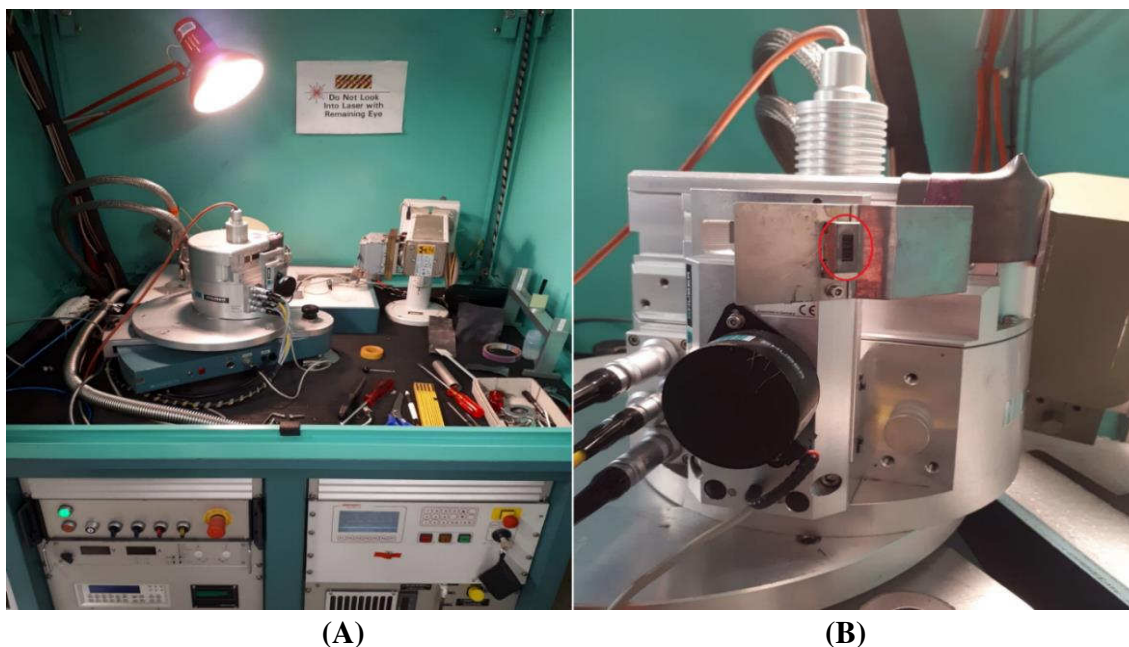
Figure 4.5: A) Photo of the Huber diffractometer at JCNS-2; B) Photo of the collimator.

The monochromatic beam is passed through the collimator, which consists of many slits with absorption layers (Soller slits) placed in front of the sample. The main purpose of these slits is to reduce the divergence of the beam (see Figure 4.5b).

The G670 Guinier camera has an integrated imaging plate detector. In addition, the housing of the G670 camera contains a laser recording unit with photomultiplier and pre-amplifier as well as a halogen lamp for deleting the recorded information on the image plate **[From: http://www.xhuber.de]**. The detection is conducted in three distinct steps: recording, reading and erasing (Figure 4.6) **[Guinebretiere, 2007]**.
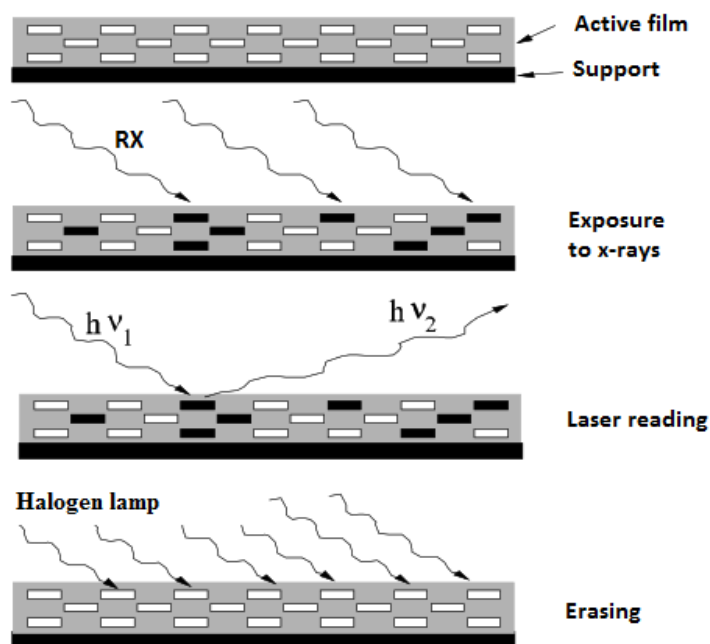
Figure 4.6: Schematic diagram of the detection steps **[Guinebretiere, 2007]**.

During exposure, the diffracted radiation from the sample hits the active part of the image plate, which is comprised of a film made of phosphorescent material ($BaFBr: Eu^{2+}$), and excites a certain number of electrons to a higher energy level (from Eu^{2+} to Eu^{3+}) **[Guinebretiere, 2007]**. Every photon scattered at the same angle will lie at the same vertical line on the imaging plate. After exposure, the image plate is scanned by a vertical linear laser beam within approximately 5 seconds.

The laser beam interacts with the excited electrons and forces them to return to the previous lower state. The photo-multiplier converts the emitted radiation to electronic current. Then, the signal is magnified by the pre-amplifier and subsequently digitalized to result in an intensity versus 2θ diagram. **[Rene Guinebretiere, 2007; From: http://www.xhuber.de]**. By means of a white halogen lamp, the signal on the image plate is deleted. After this process, the Guinier camera is ready for exposure. **[From: http://www.xhuber.de]**.

The advantage of this method is that the desired data is available within few minutes, and the amount of the sample needed for the measurements is small (several mg). In addition, this method provides a high-resolution pattern **[Cullity, 1978; David *et al*., 2002; Ladd and Palmer, 2013]**.

4.2.2 PW1050 Diffractometer (MOPS) (Reflection Geometry)

The PW1050 diffractometer, which was also used in this work, operates in a reflection Bragg-Brentano geometry. The divergent and diffracted beams from the sample surface are focused at a fixed radius from the sample position (Figure 4.7). Thus, this geometry provides reliable peak intensities and an excellent resolution due to focusing of the diffracted beam (para-focussing geometry) **[Dinnebier and Billinge, 2008]**.
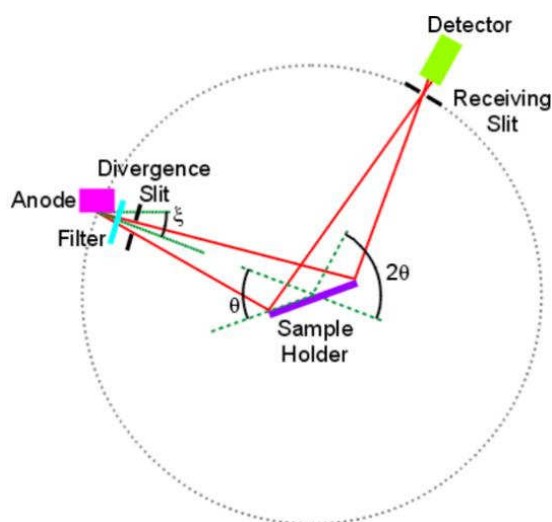
Figure 4.7: Scheme of a diffractometer setup with Bragg-Brentano geometry **[From: http://pd.chem.ucl.ac.uk]**.

Based on the moving/fixed parts, the Bragg-Brentano geometry includes two types of devices, θ-θ diffractometers and θ-2θ diffractometers. With θ-θ diffractometers, the sample does not move. The source and the detector simultaneously move in opposite directions at a speed ω. In θ-2θ diffractometers, on the other hand, the sample rotates at a speed ω, whereas the detector moves at 2ω, and the source is fixed **[Guinebretiere, 2007]**.

The PW1050 diffractometer (MOPS) (manufactured by Philips) has θ-2θ geometry and uses bi-chromatic radiation with wavelengths of 1.54060 Å (Cu Kα_1) and 1.54443 Å (Cu Kα_2). The diffractometer has a secondary monochromator in front of the detector. Figure 4.8 shows a photo of the used diffractometer in RWTH Aachen University. The X-ray optics includes a divergent slit, a receiving slit and a Soller slits at the primary beam, and an anti-scatter slit and a Soller slits at the diffracted beam **[Morawiec and Stróz, 2004]**. The monochromator is inserted at the diffracted beam, to inhibit the background that appears due to fluorescence.

29
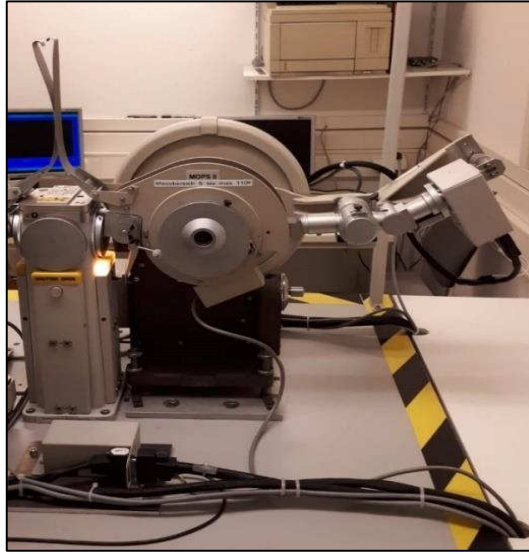
Figure 4.8: Photo of PW1050 diffractometer (MOPS) at RWTH Aachen University.

4.3 Vibrating Sample Magnetometer (VSM) for Physical Property Measurement System (PPMS)

The Physical Property Measurement System (PPMS) is an automated low-temperature and a magnet system for the measurement of material properties like specific heat, magnetic properties, and/or ac- and dc-susceptibility (see Figure 4.9). The apparatus is manufactured by QuantumDesign.

Figure 4.9: The Physical Property Measurement System used for the measurement of macroscopic magnetization data.

In the PPMS, the magnetic field can be applied up to ±9 T. The magnetic moment of the sample can be measured with a sensitivity of 10^{-9} A.m^2 (10^{-6} emu). For temperature control two options are available (standard and oven). In the case of the standard option, the temperature can be varied between 1.9 and 400 K. Using the oven option, the accessible temperature range varies from 300 to 1000 K.

The basic unit of the PPMS consists of a cryostat with a superconducting magnet coil. There are several options of the PPMS, which include Vibrating Sample Magnetometer (VSM), the AC susceptibility option (ACMSII), heat capacity and the AC resistivity option. These options result from using different measurement inserts or sample holders and require activating the according mode in the software package PPMS MultiVu. The used option for magnetization measurements performed here is VSM.

In the VSM, a homogenous magnetic field produced by superconducting magnets surrounds the inserted sample. The sample oscillates between pickup coils. The vibrating movement is driven by a linear motor. According to Faraday's law of induction, the movement of the sample induces a voltage in the pickup coils due to the change of the magnetic flux. The magnetic moment can then be calculated from this induced voltage **[(VSM) Option User's Manual]**.

Chapter Five   Experimental Methods

5.1 Synthesis of the Polycrystalline Samples of $(Mn_5Ge_3)_x(MnFe_4Si_3)_{1-x}$

The polycrystalline samples of several compositions in the pseudo-binary system $(Mn_5Ge_3)_x(MnFe_4Si_3)_{1-x}$ with $x =$ (0.2, 0.4, 0.6, 0.8) were prepared from stoichiometric amounts of the pure elements Mn (99.99% purity), Fe (99.98% purity), Ge (99.9999% purity), and Si (99.99% purity) using cold crucible induction melting (CCIM) under argon atmosphere. The mass of each sample was 5-6 g.

Figure 5.1: Photo of a crucible at the beginning of the melting process.

At first, the crucible was filled with elements choosing pieces, which were large enough to avoid them from dropping through the segments of the crucible. Then, the crucible was covered by glass and the chamber was closed tightly and evacuated to 10^{-6} mbar.

To get high purity by removing impurities (usually contamination from absorbed water), the sample was carefully heated to a temperature below the melting points of the elements under vacuum until the material started to glow and the pressure in the sample chamber was stabilized.

Afterwards, the chamber was filled with argon (pressure up to 1000 mbar), and the melting process was started (Figure 5.1). To obtain homogeneous phases, the samples were re-melted several (three to four) times. They were turned upside down in the crucible between each two melting processes. The first melting process was done fast to avoid any loss of Germanium. Subsequent melting processes took up to 5 seconds. Fast cooling of the samples was necessary to reduce segregation of the elements.

5.2 Chemical Analysis

In order to make sure that the synthesized compounds have the correct stoichiometry, chemical analysis on these compounds was performed. Two 50 mg portions of each sample, were used for testing. Every portion was dissolved in a mixture of acids (3 ml HNO_3 (65%), 3 ml HCl(30%), 3ml H_2O_2(30%), and 1ml HF(40%)) in a polystyrene falcon. Then, the volume

was increased using distilled water (up to 50 ml ≈ tube size) in order to decrease the concentration.

From each portion, two samples of approximately 100 µl each, were put in a 15 ml falcon tube, and each was mixed with 9.8 ml of water and 100 µl of $HNO_3(65\%)$. Thus, for each chemical compound, four samples were prepared for chemical analysis. The average value from the four analysis runs was used as a final value for accuracy.

The used method for analysis was Inductively Coupled Plasma-Optical Emission Spectrometry (ICP-OES), which it is a powerful technique for the analysis and quantification of trace elements in both liquid and solid samples. The analysis was performed with a iCAP 7600 ICP-OES instrument from Thermo Scientific (Figure 5.2) **[From: www.thermofisher .com]**.

In ICP-OES technique, the sample in the form of spray is introduced into the region of an ionized argon plasma which is very hot, up to 10000 °C. The hot plasma atomizes the molecules and excites the atoms to higher states. When the excited atoms return back to the ground state, they emit characteristic light of the elements **[Charles *et al.*, 2004]**.

The emitted light is split by a diffraction grating to extract the emission spectrum for the targeted elements. Detectors measure the presence or absence of the spectrum extracted for each element. The intensity of the spectrum is also detected. Thus, qualitative and quantitative analysis of the elements can be provided **[Charles *et al.*, 2004]**.

Figure 5.2: Photo of the used instrumentation for chemical analysis (iCAP 7600 ICP-OES).

5.3 X-Ray Powder Diffraction Experiment

The compounds in the system $(Mn_5Ge_3)_x(MnFe_4Si_3)_{1-x}$ were studied with monochromatic X-ray powder diffraction, to verify the phase purity of the synthesized samples, and

characterize the lattice parameters and symmetries of the major phases. These experiments were performed at room temperature.

The synthesized polycrystalline samples were polished with sand paper, to remove any contamination on the surface (usually oxidized). Then the samples were crushed and grinded in a mortar until a homogenous and very fine powder was obtained (see Figure 5.3).

| (A) | (B) |
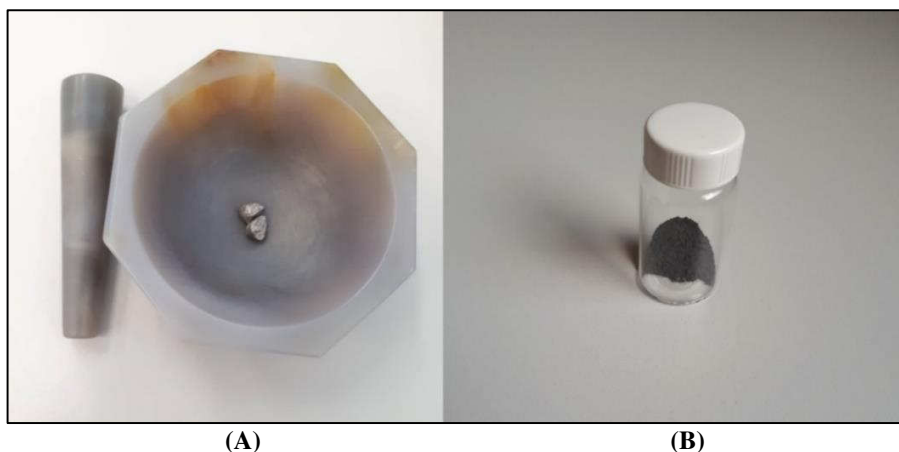
Figure 5.3: A) Ingots of the synthesized polycrystalline sample. B) The powdered sample after grinding.

5.3.1 Diffraction Experiment Using the Huber Diffractometer (G670 Guinier Camera)

For the first measurements, the powder X-ray diffraction was performed by using Cu-Kα radiation with wavelength of 1.541 Å and the data were collected on a Huber G670 Guinier camera as mentioned before. A few milligrams of powdered sample was enclosed in two sheets of foil, mixed with some drops of isopropanol for homogeneity and put into the sample holder.

As the foil is amorphous, its contribution to the powder diffraction diagram is only seen as a slight increase of the background. The holder, the metallic ring and the used spatula were cleaned by isopropanol before the use. The measurements were performed at room temperature. The total exposure time was 16-18 h per sample. To improve statistics, the sample was moved during measurement to ensure that more powder grains in more orientations are exposed to the beam. The image plate detector is scanned in the range from 0-100° with a step size of 0.005 ° to get a maximum number of 20000 measurement points.

5.3.2 Diffraction Experiment Using PW1050 Diffractometer (MOPS)

The second type of measurements were performed on a PW1050 diffractometer with CuKα_1(1.54060) and CuKα_2(1.54443) radiators. By using a spatula, few milligrams of powder were put in the holder until it was totally covered. The powder was pressed slightly by a piece of glass. The glass was removed, and the powder held on fixed without support. Then the holder was mounted in the diffractometer chamber (Figure 5.4). For each sample, the measurement was repeated three times. Every measurement took approximately 17 h. The

average of the three measurements was taken as a final result. The purpose is to reduce background and highlight the peaks. The measurements were performed at room temperature, and scanning was in the range from 10-90° with a step size of 0.02°.
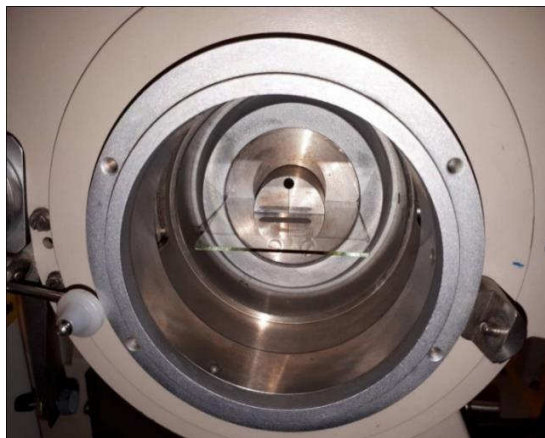
Figure 5.4: Photo of the sample chamber of the PW1050 diffractometer (MOPS) at RWTH Aachen University.

5.4 Magnetization Measurements

The mass magnetization measurements were carried out on polycrystalline samples with the weights of 9.2 mg (x = 0.8), 8.7 mg (x = 0.6), 8.6 mg (x = 0.4) and 8,9 mg (x = 0.2). Each sample was filled in a small capsule. The powder was compressed, and then the capsule was closed tightly.

The capsule was mounted on the trough-shaped sample holder (Figure 5.5a). Then, the sample position inside the capsule was adjusted manually using an external scale (called mounting station, Figure 5.5b). With care, the recommended target line at 35 ± 3 mm as a mounting location was achieved. This distance is called the sample offset **[(VSM) Option User's Manual]**. In the next step the sample holder (with the mounted sample) was removed from the mounting station and screwed onto the end of the sample rod. The rod then was inserted into the PPMS sample chamber.

(A) **(B)**
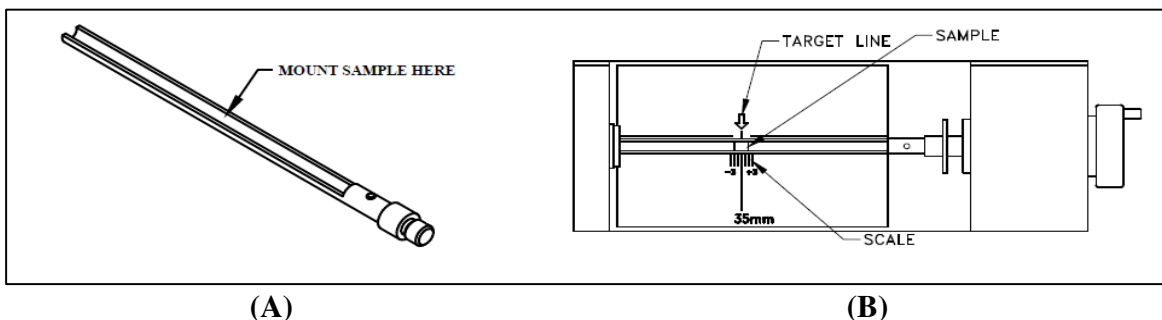
Figure 5.5: A) Trough-shaped sample holder; B) Reading the position of the sample from the sample-mounting station **[(VSM) Option User's Manual]**.

In the next step, the sample was centred at the proper position, and this was confirmed using a small field of 100 Oe. The position was confirmed to be within the range 35 ± 3 mm (Figure 5.6). Finally, the specific measurement sequences were created, e.g., the field, the temperature range and the intervals for the measurements (Appendix Table A.1).
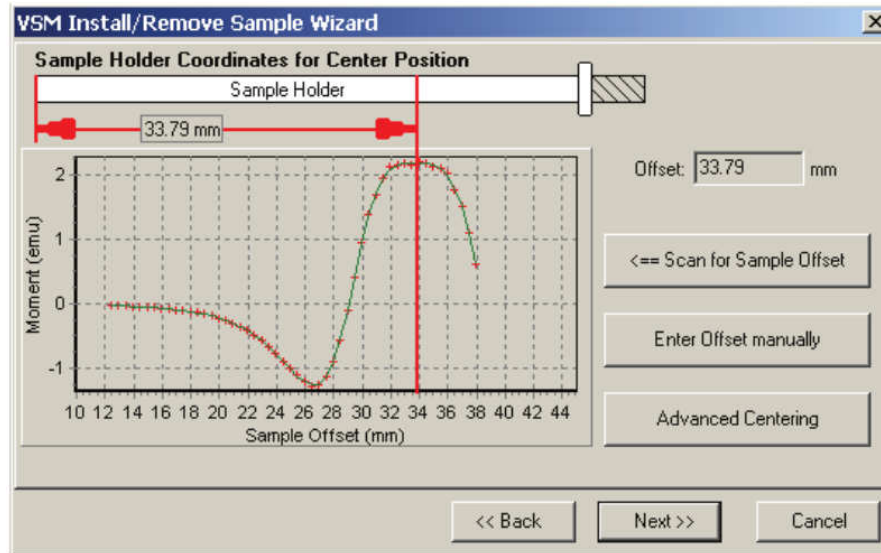
Figure 5.6: Determining the sample offset for the magnetization measurements **[(VSM) Option User's Manual]**.

Chapter Six   Results and Discussion

6.1 Stoichiometry of the Synthesized Samples Based on Chemical Analysis

Tables 6.1 and 6.2 summarize the results from the chemical analysis. In addition to the expected elements (Mn, Fe, Si, Ge), the copper content of the samples was also checked to make sure that there was no contamination from the crucible. The percentage of copper in all samples is negligible (see Table 6.1).

Table 6.1: Weight percent of the elements with standard deviation for the different samples according to the chemical analysis- Averaged values from 4 independent analysis runs.

	$Mn_{4.2}Ge_{2.4}Fe_{0.8}Si_{0.6}$ $x = 0.8$	$Mn_{3.4}Ge_{1.8}Fe_{1.6}Si_{1.2}$ $x = 0.6$	$Mn_{2.6}Ge_{1.2}Fe_{2.4}Si_{1.8}$ $x = 0.4$	$Mn_{1.8}Ge_{0.6}Fe_{3.2}Si_{2.4}$ $x = 0.2$
Weight % of Fe	9.81(4)	20.28(9)	46.32(12)	32.59(18)
Weight % of Ge	33.21(11)	26.876(97)	10.82(3)	19.66(14)
Weight% of Mn	49.7(2)	42.3(2)	25.34(5)	34.3(2)
Weight % of Si	3.653(10)	7.72(2)	17.66(4)	12.34(6)
Weight % of Cu	< 0.0009	< 0.001	< 0.001	< 0.001

Table 6.2 shows the difference between the calculated stoichiometry and the obtained values according to the analysis. All samples show a small deficiency of Ge and the first two samples ($x = 0.8$, $x = 0.6$) show a slight excess of Mn. However, altogether the results from the analysis are in good agreement with expectations.

Table 6.2: Comparison of the ideal stoichiometry and the stoichiometry resulting from the chemical analysis for the synthesis products in the system $(Mn_5Ge_3)_x(MnFe_4Si_3)_{1-x}$.

x parameter	Ideal stoichiometry	Formula according to the results from the chemical analysis
0.8	$Mn_{4.2}Ge_{2.4}Fe_{0.8}Si_{0.6}$	$Mn_{4.38(2)}Ge_{2.216(7)}Fe_{0.852(3)}Si_{0.615(2)}$
0.6	$Mn_{3.4}Ge_{1.8}Fe_{1.6}Si_{1.2}$	$Mn_{3.491(1)}Ge_{1.678(2)}Fe_{1.647(7)}Si_{1.246(3)}$
0.4	$Mn_{2.6}Ge_{1.2}Fe_{2.4}Si_{1.8}$	$Mn_{2.62(2)}Ge_{1.135(8)}Fe_{2.45(1)}Si_{1.843(9)}$
0.2	$Mn_{1.8}Ge_{0.6}Fe_{3.2}Si_{2.4}$	$Mn_{1.790(4)}Ge_{0.578(2)}Fe_{3.218(8)}Si_{2.440(6)}$

6.2 Determination of the Crystal Structure

6.2.1 LeBail Refinement of the Powder Diffraction Data

After data acquisition from both powder diffractometers, LeBail refinements were performed on the powder diagrams of the samples to obtain the lattice parameters and preliminary information about the space group of the compounds. In addition, the LeBail refinement in this case also provided information about the number of crystalline phases in the synthesized products. The refinements were carried out with the program Jana 2006 **[Petříček *et al.*, 2014]**, a crystallographic program for the refinement of crystal structures from powder and single crystal data.

In order to fit the observed profile, two phases (at least) must be considered for all samples. For the first phase, the lattice parameters of Mn_5Ge_3 (space group $P6_3/mcm$) were used as a

starting model **[Forsyth and Brown, 1990]**. The lattice parameters where then manually changed while visually inspecting the pattern until the calculated peak positions were in approximate agreement with the observed ones. As it was not possible to index all peaks with the lattice parameters of this first phase, the same procedure was repeated to obtain good starting parameters for the second phase (assuming space group $P6_3/mcm$). The lattice parameters for both phases were subsequently refined.

In some of the patterns, very few additional weak peaks were visible, which correspond to an additional impurity phase. Several impurity phases were tested for refinement. However, as the fitting using these phases did not significantly improve, they were eventually omitted. This is in agreement with earlier investigations on the quaternary system $Mn_{5-x}Fe_xGeSi_2$ with $x = 1.5$ and 2, where a co-existence of two phases was also observed **[Sun *et al.*, 2017]**.

For the data from the Huber diffractometer, the peak shapes of $Mn_{4.2}Ge_{2.4}Fe_{0.8}Si_{0.6}$ and $Mn_{3.4}Ge_{1.8}Fe_{1.6}Si_{1.2}$ were refined as pseudo-Voigt functions. As the introduction of the Gaussian parameter GW did not lead to a good fit of the data, the angle dependent parameter GU (denoted U in Cagliotti equation) was used as a fit parameter for the Gaussian part (see equation 2.6). For the Lorentzian part, LX was used as the fit parameter. For $Mn_{2.6}Ge_{1.2}Fe_{2.4}Si_{1.8}$ and $Mn_{1.8}Ge_{0.6}Fe_{3.2}Si_{2.4}$, a pure Lorentzian function using LX as a free parameter was sufficient to describe the peak shape. The cut-off distance was 8 FWHM for all phases in all refinements.

The GU and LX parameters for the two phases, which were taken into account in one refinement were restricted to be equal, as this is a reasonable assumption and reduces the number of parameters in the refinement. The zero-shift correction was also refined for the first three samples. The background was fitted manually by using about 30-45 points.

Due to problems during the measurement on the second diffractometer (PW1050 diffractometer), only the data for two of the samples ($x = 0.8$ and 0.6) was available. The peak shapes were refined by pseudo-Voigt function for the first sample, and a Gaussian for the second one. For the first sample, GU was used as a fit parameter for the Gaussian part, and LX was used as a fit parameter for the Lorentzian part. For the second sample, both GU and GW were used as free parameters.

The cut-off distance was 8 FWHM for the two samples. As before, the free parameters GU, GW and LX were restricted to be equal for the two phases, which had to be taken into account in the refinement. The zero-shift correction was also refined for the first sample ($x = 0.8$), and was zero for the second sample ($x = 0.6$). The background was fitted manually by using 60 points for the first sample and around 90 points for the second sample.

Figures 6.1 and 6.2 show representative results of a LeBail refinement for $Mn_{4.2}Ge_{2.4}Fe_{0.8}Si_{0.6}$ from Jana 2006, for the data from the Huber diffractometer and PW1050 diffractometer, respectively. The results of the other samples are shown in the appendix A. The observed profile is shown in black, while the calculated profile is shown in red. The difference profile is shown at the bottom. Vertical tick-marks indicate the peak position of the calculated reflections. The values of R_{wp} and R_p for all refinements are given in Table 6.3 for the Huber diffractometer data, and Table 6.4 for the PW1050 diffractometer data.
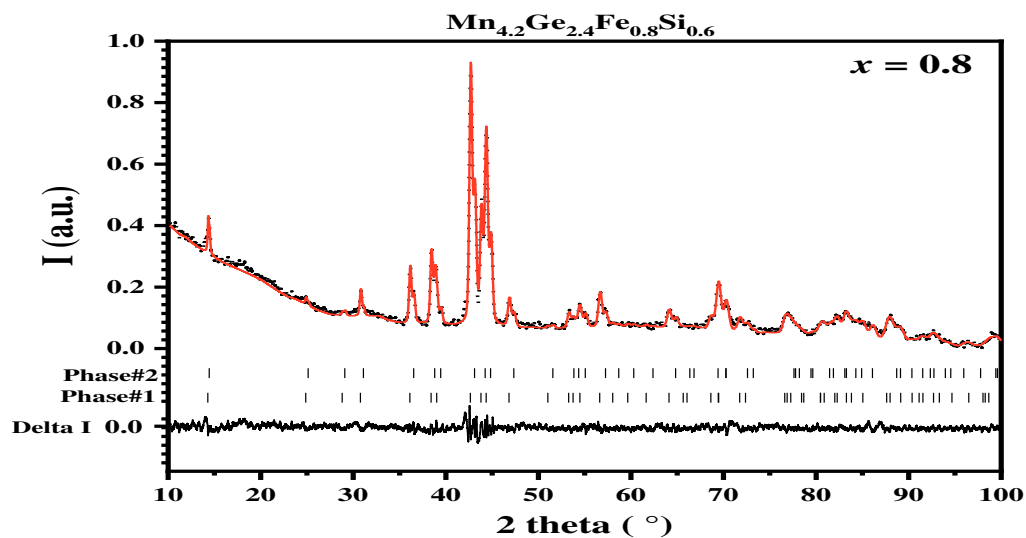
Figure 6.1: Observed (black) and calculated (red) profiles using the LeBail method for $Mn_{4.2}Ge_{2.4}Fe_{0.8}Si_{0.6}$ based on the data from the Huber diffractometer.
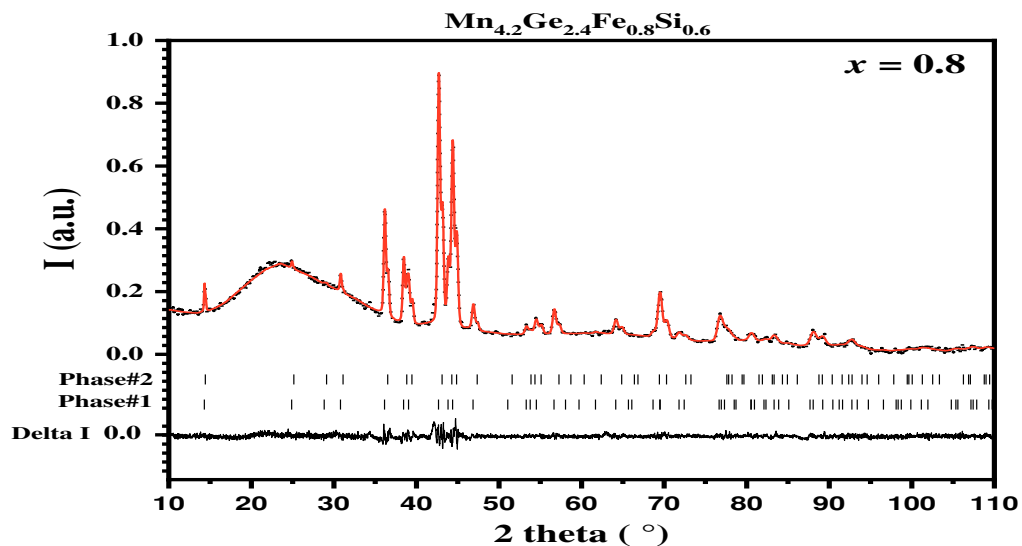
Figure 6.2: Observed (black) and calculated (red) profiles using the LeBail method for $Mn_{4.2}Ge_{2.4}Fe_{0.8}Si_{0.6}$ based on the data from the PW1050 diffractometer.

Table 6.3: R-factors for the LeBail refinements of the data measured on the Huber diffractometer.

Compound	R_{wp} (%)	R_p
$Mn_{4.2}Ge_{2.4}Fe_{0.8}Si_{0.6}$	1.18	0.89
$Mn_{3.4}Ge_{1.8}Fe_{1.6}Si_{1.2}$	1.11	0.81
$Mn_{2.6}Ge_{1.2}Fe_{2.4}Si_{1.8}$	1.11	0.81
$Mn_{1.8}Ge_{0.6}Fe_{3.2}Si_{2.4}$	0.95	0.68

Table 6.4: R-factors for the LeBail refinements of the data measured on the PW1050 diffractometer.

compound	R_{wp} (%)	R_p
$Mn_{4.2}Ge_{2.4}Fe_{0.8}Si_{0.6}$	4.08	2.93
$Mn_{3.4}Ge_{1.8}Fe_{1.6}Si_{1.2}$	4.17	2.84

Unit cell parameters, shift correction, *c /a* ratio, and the volume of the unit cells resulting from the LeBail fits together with the corresponding parameters of the end members are presented in the Tables 6.5 and 6.6, for the data from the Huber diffractometer and PW1050 diffractometer, respectively. *c/a* values from both diffractometers are comparable. The lattice parameters and volumes of the unit cells against the compositional parameter *x* are shown in Figure 6.3 and Figure 6.4. The unit cell parameters values for *x* = 0.8 in the two phases are close to those reported by **Halder *et al.* [2011]** for the compound $Mn_4Ge_{2.4}FeSi_{0.6}$ which has a similar stoichiometry.

Table 6.5: Unit cell parameters, zero shift correction, *c/a* ratio, and the volume of the unit cells resulting from the LeBail refinements of the patterns measured with the Huber diffractometer. **[(1): Forsyth and Brown, 1990; (2): Hering *et al*., 2015]**.

Compound	Phase no.	$a = b$ (Å)	c (Å)	c/a ratio	V (A³)	Shift correction
Mn_5Ge_3 [1]		7.184(2)	5.053(2)	0.7034(3)	225.85	
$Mn_{4.2}Ge_{2.4}Fe_{0.8}Si_{0.6}$	Phase1	7.153(2)	4.970(2)	0.6948(3)	220.2(2)	-5.3(1.6)
	Phase2	7.084(3)	4.917(2)	0.6941(4)	213.7(1)	
$Mn_{3.4}Ge_{1.8}Fe_{1.6}Si_{1.2}$	Phase1	7.111(5)	4.929(4)	0.6932(7)	215.9(3)	-8.2(2.9)
	Phase2	6.968(5)	4.827(4)	0.6927(8)	203.0(3)	
$Mn_{2.6}Ge_{1.2}Fe_{2.4}Si_{1.8}$	Phase1	7.023(4)	4.863(5)	0.6924(8)	207.7(3)	-4.6(2.7)
	Phase2	6.895(4)	4.782(3)	0.6935(6)	196.9(3)	
$Mn_{1.8}Ge_{0.6}Fe_{3.2}Si_{2.4}$	Phase1	7.094(1)	4.879(2)	0.6878(3)	212.63(3)	0
	Phase2	6.8445(7)	4.7513(8)	0.6942(1)	192.76(3)	
$MnFe_4Si_3$ [2]		6.8011(1)	4.7307(1)	0.69560(2)	189.50	

Table 6.6: Unit cell parameters, shift correction, *c/a* ratio and the volume of the unit cells of the refined pattern using data from the PW1050 diffractometer.

Compound	Phase no.	$a = b$ (Å)	c (Å)	c/a ratio	V (A³)	Shift correction
$Mn_{4.2}Ge_{2.4}Fe_{0.8}Si_{0.6}$	Phase1	7.150(1)	4.9675(9)	0.6948(2)	219.90(7)	- 3.9(7)
	Phase2	7.081(1)	4.917(1)	0.6944(2)	213.49(7)	
$Mn_{3.4}Ge_{1.8}Fe_{1.6}Si_{1.2}$	Phase1	7.0990(8)	4.9176(9)	0.6927(1)	214.62(4)	0
	Phase2	6.962(1)	4.8202(9)	0.6924(2)	202.31(4)	
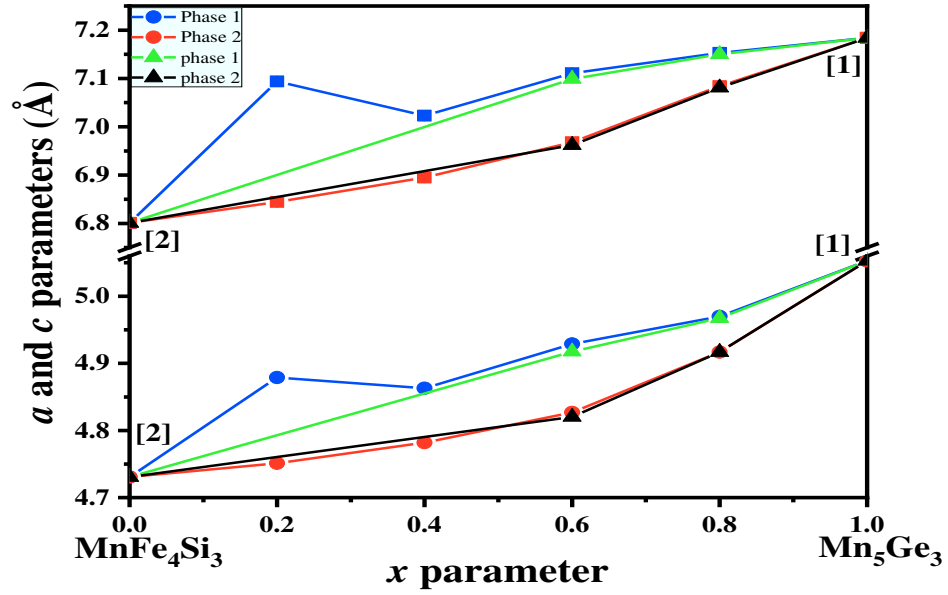
Figure 6.3: Change of Lattice parameters in dependence of the compositional parameter *x* of the series of $(Mn_5Ge_3)_x(MnFe_4Si_3)_{1-x}$. **[[1]: Forsyth and Brown, 1990; [2]: Hering *et al*., 2015]**. Symbols are larger than the error bars. Symbols in blue and red are for data from the Huber diffractometer. Symbols in green and black are for data from the PW1050 diffractometer.
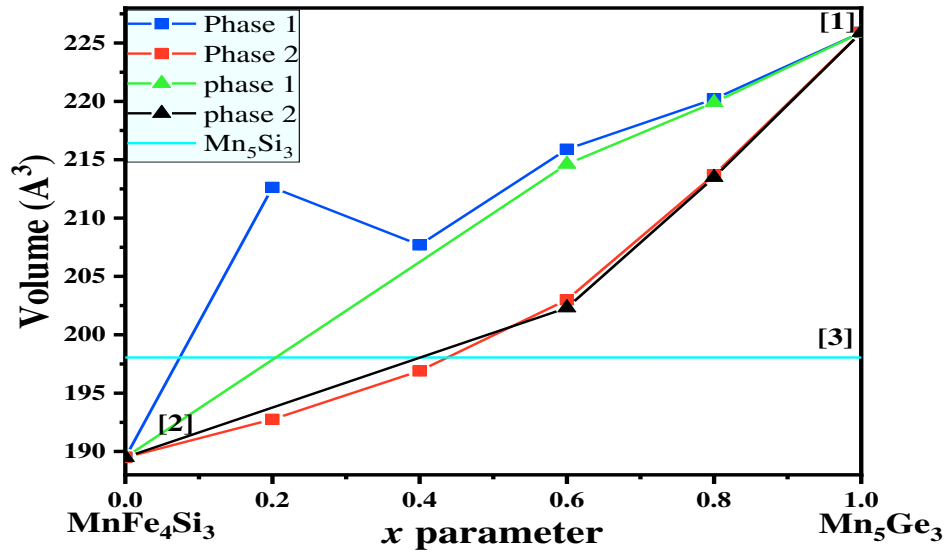
Figure 6.4: Change of unit cell volume as a function of the compositional parameter *x* of the series of $(Mn_5Ge_3)_x(MnFe_4Si_3)_{1-x}$. **[[1]: Forsyth and Brown, 1990; [2]: Hering *et al*., 2015; [3]: Yusupov *et al*., 2009].** Symbols are larger than the error bars. Symbols in blue and red are for data from the Huber diffractometer. Symbols in green and black are for data from the PW1050 diffractometer.

For phase one, the lattice parameters and the volume decrease with decreasing of *x* parameter. This is consistent with the smaller atom radius of Si compared to Ge, in agreement with

earlier results for $Mn_4FeGe_{3-y}Si_y$ **[Halder *et al.*, 2011]**. Similarly, the comparison of Fe to Mn agrees with the earlier results for $Mn_{5-x}Fe_xGeSi_2$ **[Sun *et al.*, 2017]**. However, they have a larger value at $x = 0.2$. For phase two, the lattice parameters and volume decrease with the decrease in x parameter. In phase one, all samples must have incorporated Ge, because the unit cell volume is larger than that of Mn_5Si_3, and only Ge can produce this effect. For phase two, at least two samples ($x = 0.8$ and 0.6) must have incorporated Ge. The c/a ratio remains more or less constant for the two phases, indicating a uniform contraction of the unit cell volume.

6.2.2 Rietveld Refinement

To obtain detailed information about the crystal structure of the compounds, data using the PW1050 diffractometer were refined with the Rietveld method. The coordinates of Mn_5Ge_3 atoms **[Forsyth and Brown, 1990]** were used as an initial model for the Ge-rich samples, and the coordinates of $MnFe_4Si_3$ atoms **[Hering *et al.*, 2015]** were used as an initial model for the Si-rich samples. Lattice parameters and all other initial values were taken from the LeBail refinement. In addition to the atomic coordinates, the phase volume fractions, isotropic atomic displacement parameters, and the preferred orientation [0 0 1] according to March-Dollase were also refined **[March, 1932; Dollase, 1986]**.

For each sample, GU, GW, LX, and the preferred orientation parameter, were restricted to be equal for the two phases. Figure 6.5 shows a representative result of Rietveld refinement for $Mn_{4.2}Ge_{2.4}Fe_{0.8}Si_{0.6}$ from Jana 2006. The results for $Mn_{3.4}Ge_{1.8}Fe_{1.6}Si_{1.2}$ are shown in Figure A.5 of appendix A. The values of R_{wp} and R_p for the Rietveld refinements are given in Table 6.7, for PW1050 diffractometer data.
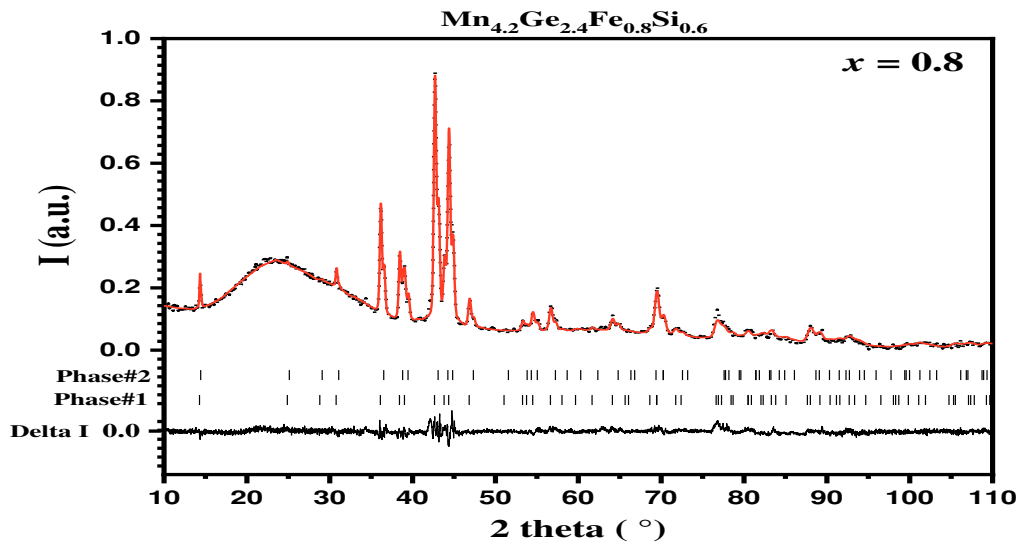
Figure 6.5: Observed (black) and calculated (red) profiles using the Rietveld method for $Mn_{4.2}Ge_{2.4}Fe_{0.8}Si_{0.6}$ based on the data from the PW1050 diffractometer.

Table 6.7: R-factors for the Rietveld refinements of the data measured on the PW1050 diffractometer.

compound	R_{wp} (%)	R_p
$Mn_{4.2}Ge_{2.4}Fe_{0.8}Si_{0.6}$	4.79	3.38
$Mn_{3.4}Ge_{1.8}Fe_{1.6}Si_{1.2}$	5.15	3.35

The atom type, x, y, z coordinates, isotropic thermal parameter, and occupancy factor are listed in Table 6.8. As expected, the lattice parameters and the zero-shift parameter are hardly different from the ones obtained from the LeBail fit (Table 6.9). The refined volume fractions of both phases are also listed in Table 6.9. In the refinements, Mn and Fe were treated as Mn. This was justified because the two elements have only one electron difference and are basically indistinguishable in X-ray diffraction. The samples with $x = 0.8$ and $x = 0.6$ crystallize in the space group $P6_3/mcm$.

Table 6.8: Atom type, x, y, z coordinate, isotropic thermal parameter, and the occupancy factor based on the data from the PW1050 diffractometer.

Compound	Phase no.	Atom type	x, y, z coordinates	Isotropic thermal parameter	Occupancy factor
$Mn_{4.2}Ge_{2.4}Fe_{0.8}Si_{0.6}$	Phase1	Mn1	0.333333, 0.666667, 0	0.046(2)	0.166667
		Mn2	0.2313(4), 0, 0.25	0.0212(9)	0.25
		Ge	0.5996(3), 0, 0.25	0.0120(7)	0.199(3)
		Si	0.5996, 0, 0.25	0.012	0.051385
	Phase2	Mn1	0.333333, 0.666667, 0	0.046	0.166667
		Mn2	0.2330(8), 0, 0.25	0.0212	0.25
		Ge	0.6039(8), 0, 0.25	0.012	0.141(5)
		Si	0.6039, 0, 0.25	0.012	0.109107
$Mn_{3.4}Ge_{1.8}Fe_{1.6}Si_{1.2}$	Phase1	Mn1	0.333333, 0.666667, 0	0.040(2)	0.166667
		Mn2	0.2383(5), 0, 0.25	0.022(1)	0.25
		Ge	0.6058(6), 0, 0.25	0.044(2)	0.214(6)
		Si	0.605788, 0, 0.25	0.044	0.036190
	Phase2	Mn1	0.333333, 0.666667, 0	0.04	0.166667
		Mn2	0.2396(8), 0, 0.25	0.022	0.25
		Ge	0.607(1), 0, 0.25	0.044	0.112(7)
		Si	0.607, 0, 0.25	0.044	0.137579

Table 6.9: Lattice parameters, zero shift correction, c/a ratio, volume of the unit cell and refined phase volume fractions based on the data from the PW1050 diffractometer.

Compound	Phase no.	$a = b$ (Å)	c (Å)	c/a ratio	V (Å^3)	Shift correction	phase volume fractions
$Mn_{4.2}Ge_{2.4}Fe_{0.8}Si_{0.6}$	Phase1	7.1523(5)	4.9696(4)	0.6948(7)	220.16(3)	-5.5(3)	0.656(4)
	Phase2	7.0853(6)	4.9177(5)	0.6941(9)	213.80(3)		0.344(4)
$Mn_{3.4}Ge_{1.8}Fe_{1.6}Si_{1.2}$	Phase1	7.0992(4)	4.9200(4)	0.6930(7)	214.74(2)	0	0.545(5)
	Phase2	6.9549(5)	4.8211(5)	0.6932(9)	201.96(2)		0.455(5)

For each phase, the sum of the occupancies of Ge and Si was set to the ideal value, yet their ratio was refined for each individual phase. The ratio of Ge to Si as obtained from the

Rietveld refinement was then calculated. As can be seen, the values are significantly different from the ones obtained from chemical analysis (Table 6.10).

Table 6.10: Ratio of Germanium to Silicon from powder refinements and chemical analysis.

Compound	Ge/Si calculated from powder pattern	Ge/Si based on chemical analysis
$Mn_{4.2}Ge_{2.4}Fe_{0.8}Si_{0.6}$	2.51	3.603
$Mn_{3.4}Ge_{1.8}Fe_{1.6}Si_{1.2}$	2.037	1.347

6.3 Analysis of the Magnetization Measurements

In order to investigate the magnetic properties of the compounds in the system $(Mn_5Ge_3)_x(MnFe_4Si_3)_{1-x}$, magnetization measurement as a function of temperature (isofield magnetization measurements) were performed, using two modes: Field cooling (FC) and field warming (FW). During the FC measurement, a magnetic field of 0.1 T was applied to the sample and then magnetization was measured while cooling the sample from 390 to 20 K. At 20 K, a hysteresis measurement was performed for the sample with ±8 T. Afterward, the field was reduced from 8 to 0.1 T, and the sample magnetization was measured again, while increasing the temperature from 20 to 390 K (FW measurement). This protocol for the FC-FW measurement was used for all the samples. At selected temperatures, further isothermal measurements within the field range of ± 8 T were performed.

6.3.1 Isofield Magnetization Measurements of Compounds in the System $(Mn_5Ge_3)_x(MnFe_4Si_3)_{1-x}$

Figure 6.6 shows the temperature dependence of magnetization for the compounds in the system $(Mn_5Ge_3)_x(MnFe_4Si_3)_{1-x}$. A split between the field cooling and warming curves is seen in all samples. The response difference upon heating and cooling is most likely due to the temperature-field protocol of the measurement, as a hysteresis loop from -8 to +8 T was measured between the two isofield measurements. The magnetization was observed to be inversely proportional to temperature for all the samples.

For the first sample, $Mn_{4.2}Ge_{2.4}Fe_{0.8}Si_{0.6}$ (x = 0.8), the magnetic response exhibits only a weak temperature dependence. At ~270 K the magnetization starts to decrease strongly. At 295 K, the FC and FW cross, and above 350 K, the split narrows, with very small difference. This behaviour above 350 K is similar for all samples. However, magnetization in the case of FW were always larger than the FC values for the second, third and fourth samples.

The curves in the case above (x = 0.8) saturate and show approximately constant magnetization in the temperature range below ~ 265 K. However, there is a very shallow maximum at 105 K (Figure 6.7). The gradient is large between 280 and 320 K.
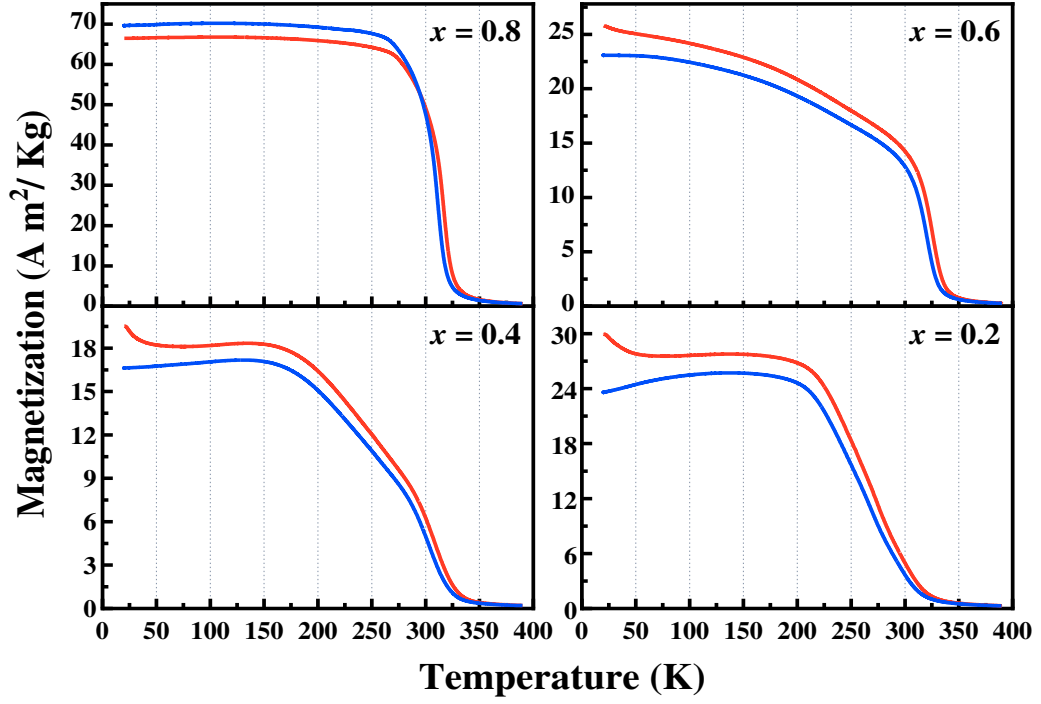
Figure 6.6: Temperature dependence of magnetization of the compounds in the system $(Mn_5Ge_3)_x(MnFe_4Si_3)_{1-x}$, measured in $\mu_0H = 0.1$ T. Blue curves represent FC and red curves represent FW.
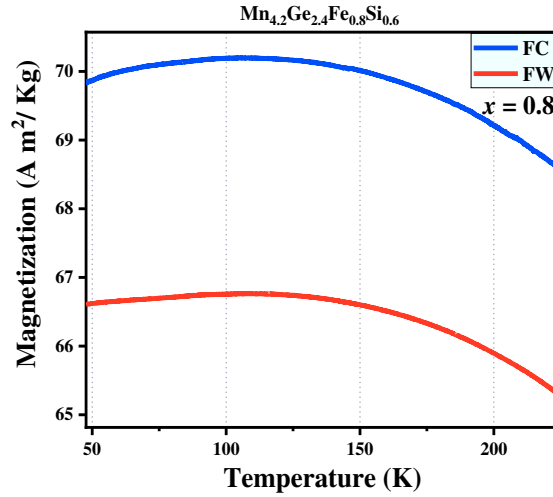
Figure 6.7: Temperature dependence of magnetization of $Mn_{4.2}Ge_{2.4}Fe_{0.8}Si_{0.6}$.

For the second sample, $Mn_{3.4}Ge_{1.8}Fe_{1.6}Si_{1.2}$ ($x = 0.6$), magnetization in a field of 0.1 T decreases monotonically within the studied temperature range. We identify two regions with a nearly constant gradient, the first one between 180 and 270 K and the second one between

45

305 and 325 K. Above 350 K, field cooling and warming curves approach each other. Magnetization values for this compound are smaller than those of the first compound at 0.1 T.

The third sample, $Mn_{2.6}Ge_{1.2}Fe_{2.4}Si_{1.8}$ ($x = 0.4$), behaves very similar to the $x = 0.6$ sample above 150 K with two rather linear regions. However, the low temperature behaviour is clearly distinct from the former samples, as the magnetization features a maximum at ~ 150 K. Magnetization values for this compound are smaller than the ones observed in the previous samples at 0.1 T.

In the fourth compound, $Mn_{1.8}Ge_{0.6}Fe_{3.2}Si_{2.4}$ ($x = 0.2$), magnetization decreases fairly linear from 210 to 290 K. The field cooling and warming curves feature a maximum similar to the $x = 0.4$ sample. The magnetic response to a field of 0.1 T is stronger than the case of $x = 0.6$ and 0.4.

The transition temperatures were estimated using the crossing point of two straight lines fitted to the region above and below the transition temperature (see Figure 6.8). In all samples, the transition temperatures in the case of field cooling differ from the ones of field warming. Therefore, all samples have a thermal hysteresis which amounts approximately to 5 K. Table 6.11 shows the transition temperatures in the case of FC and FW. The thermal hysteresis indicates the character of first order phase transitions.
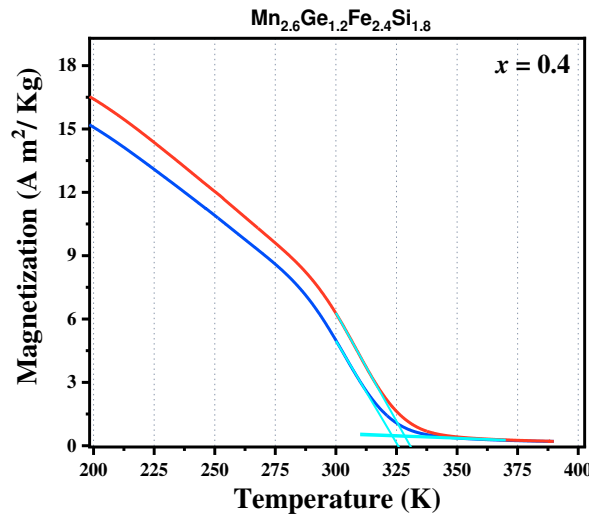
Figure 6.8: Fitting of linear functions to extract transition temperatures for $Mn_{2.6}Ge_{1.2}Fe_{2.4}Si_{1.8}$.

The transition temperatures decrease with the decrease in x parameter from 0.6 to 0.2, i.e. increasing Fe and Si content. However, the transition temperatures of the first sample ($x = 0.8$) are lower than those for the samples with $x = 0.6$ and 0.4.

Table 6.11: Transition temperatures in the case of FC and FW for the compounds in the system $(Mn_5Ge_3)_x(MnFe_4Si_3)_{1-x}$.

Compound	Transition temperature (K)	
	FC	FW
$Mn_{4.2}Ge_{2.4}Fe_{0.8}Si_{0.6}$	319.6 (2.5)	325.1 (2.4)
$Mn_{3.4}Ge_{1.8}Fe_{1.6}Si_{1.2}$	331.3 (3.3)	336.8 (4.3)
$Mn_{2.6}Ge_{1.2}Fe_{2.4}Si_{1.8}$	323.4 (2.3)	328.3 (2.6)
$Mn_{1.8}Ge_{0.6}Fe_{3.2}Si_{2.4}$	308.3 (2.2)	313.4 (2.5)

We tried to derive the Curie parameter and the effective paramagnetic moment from a Curie-Weiss analysis of the high temperature part of the susceptibility. We fitted a linear function to the inverse of susceptibility in the temperature range 370 K < T < 390 K. The resulting effective paramagnetic moment exceeds the value of 5 μ_B per transition metal ion significantly. Therefore, we conclude that we are not yet in the Curie-Weiss regime, but short-range correlations still exist. Meanwhile, measurements at higher temperatures were not investigated in this work.

6.3.2 Isothermal Magnetization Measurements of Compounds in the System $(Mn_5Ge_3)_x(MnFe_4Si_3)_{1-x}$

Figure 6.9 shows isothermal magnetization measurements for the compounds in the system $(Mn_5Ge_3)_x(MnFe_4Si_3)_{1-x}$ at different temperatures. The field dependence for the second, third and fourth samples at further temperatures are shown in Figures A.6 to A.8, in appendix A. For the first sample ($x =0.8$), the field was applied only from 8 to -8 T (two quadrants) for temperatures from 350 to 300 K. For the other temperatures and for the other samples, the applied field was from 8 to -8 T and then returned back again to 8 T.

At low temperature, the sample $Mn_{4.2}Ge_{2.4}Fe_{0.8}Si_{0.6}$ ($x = 0.8$) saturates in a field $\mu_0H \approx 1$ T. The saturation magnetization exceeds 250 Am^2kg^{-1} at 20K, which is hard to understand. For $Mn_{3.4}Ge_{1.8}Fe_{1.6}Si_{1.2}$ ($x = 0.6$), the magnetization approaches saturation at a larger field. The value of the saturation magnetization at 20 K approaches 130 Am^2kg^{-1}.

In the case of $Mn_{2.6}Ge_{1.2}Fe_{2.4}Si_{1.8}$ ($x = 0.4$), saturation is approached at even larger fields. The magnetization increases still upon application of an 8 T field at 20 K. The value of magnetization at maximum field at 20 K are slightly smaller than the magnetization of the $x = 0.6$ sample.
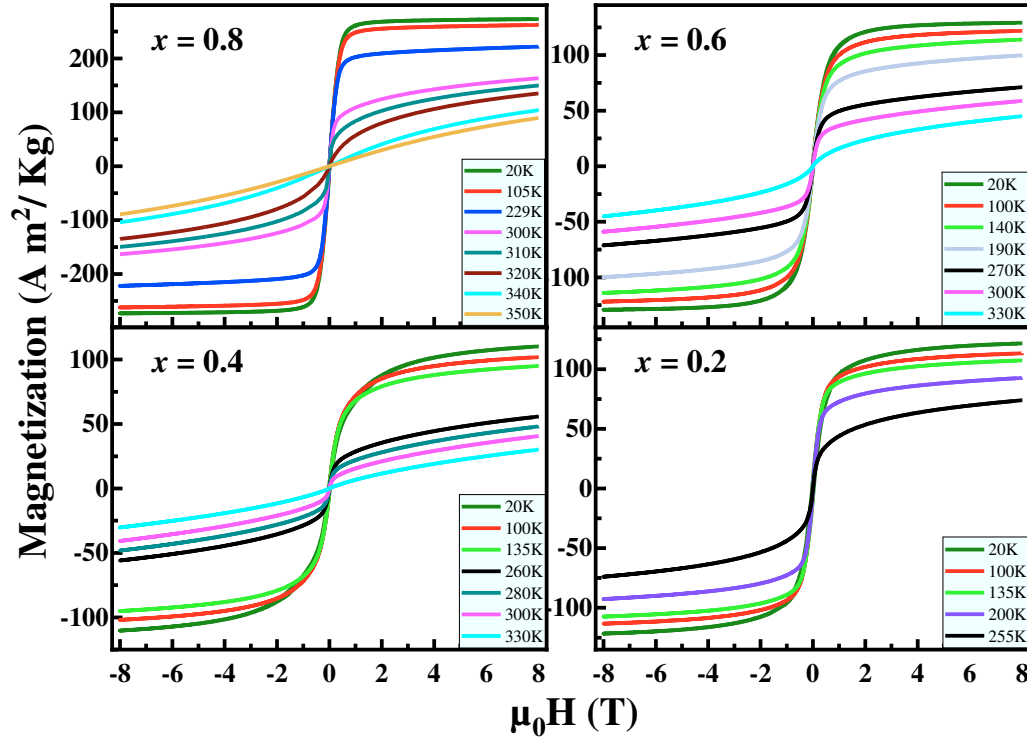
Figure 6.9: Isothermal measurements of magnetization of the compounds in the system $(Mn_5Ge_3)_x(MnFe_4Si_3)_{1-x}$ at different temperatures.

For $Mn_{1.8}Ge_{0.6}Fe_{3.2}Si_{2.4}$ ($x = 0.2$), the M(H) curves have a similar shape as the $x = 0.6$ sample. The saturation magnetization is slightly higher than in the $x = 0.4$ case. While for the first three samples the saturation magnetization decreases with decreasing x, in this sample it increases. Also, the saturation is approached faster than in the $x = 0.4$ case. Table 6.12 presents the saturation magnetization at the base temperature.

Table 6.12: Saturation magnetization at the base temperature of the compounds in the system $(Mn_5Ge_3)_x(MnFe_4Si_3)_{1-x}$.

Compound	Saturation magnetization at 20K (μ_B/ f.u.)
$Mn_{4.2}Ge_{2.4}Fe_{0.8}Si_{0.6}$	22.5
$Mn_{3.4}Ge_{1.8}Fe_{1.6}Si_{1.2}$	10.2
$Mn_{2.6}Ge_{1.2}Fe_{2.4}Si_{1.8}$	8.2
$Mn_{1.8}Ge_{0.6}Fe_{3.2}Si_{2.4}$	8.5

In the case of $Mn_{2.6}Ge_{1.2}Fe_{2.4}Si_{1.8}$ ($x = 0.4$), the values of magnetization at 20 and 25 K are more or less the same at very low field. By increasing the field, the magnetization at 25 K becomes higher than at 20 K. At higher fields, the difference decreases, but it still remains slightly higher for 25 K (see Figure 6.10).

48
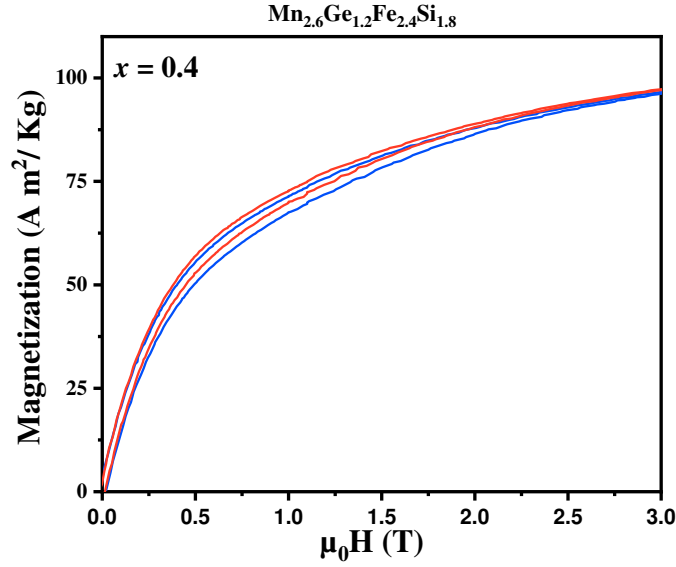
Figure 6.10: Temperature dependence of magnetization of $Mn_{2.6}Ge_{1.2}Fe_{2.4}Si_{1.8}$ under 20K (blue colour) and 25K (red colour).

The samples with $x = 0.8$ and $x = 0.6$ do not show significant magnetic hysteresis, i.e. the curves for increasing and decreasing the field coincide, while for $Mn_{2.6}Ge_{1.2}Fe_{2.4}Si_{1.8}$ and $Mn_{1.8}Ge_{0.6}Fe_{3.2}Si_{2.4}$, the loops are open at low temperature up to 35 K. Table 6.13 shows the coercive field for the temperature range.

Table 6.13: Coercive field of $Mn_{2.6}Ge_{1.2}Fe_{2.4}Si_{1.8}$ and $Mn_{1.8}Ge_{0.6}Fe_{3.2}Si_{2.4}$ in the temperature range from 20 to 35 K with 5 K step.

Compound	Temperature (K)	Coercive field (mT)
$Mn_{2.6}Ge_{1.2}Fe_{2.4}Si_{1.8}$	20	17 (5)
	25	14 (5)
	30	12 (5)
	35	10 (5)
$Mn_{1.8}Ge_{0.6}Fe_{3.2}Si_{2.4}$	20	34 (5)
	25	29 (5)
	30	27 (5)
	35	23 (5)

As can be seen from Fig. 6.11, the hysteric behaviours of the sample $x = 0.4$ and $x = 0.2$ are different. In the latter case the coercive field at 20 K has a value $\mu_0 H_C = 34$ mT. The loop has the widest opening around zero field. In the case of $x = 0.4$ the situation is different. While it exhibits also a finite coercive field $\mu_0 H_C = 17$ mT at 20K, the difference between ramping the field up and down is largest in the field region around 1 T.
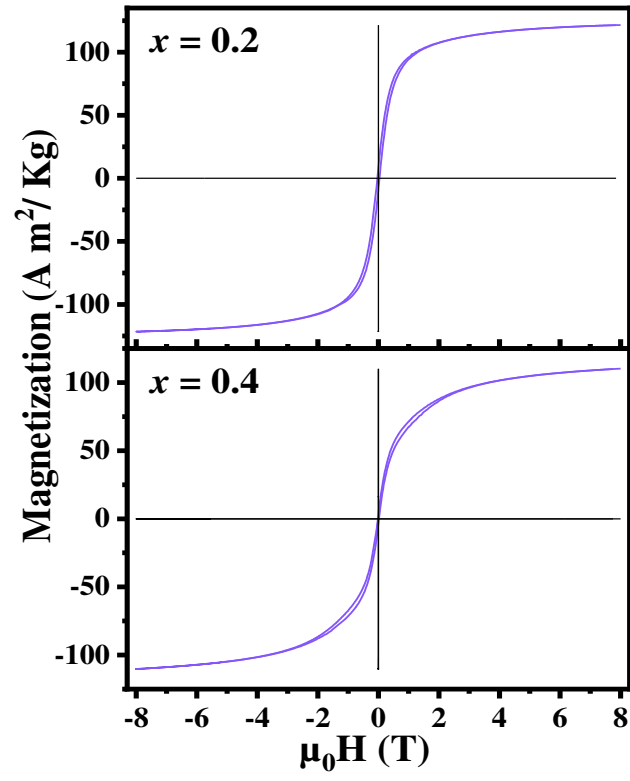
Figure 6.11: Hysteresis loop for $Mn_{2.6}Ge_{1.2}Fe_{2.4}Si_{1.8}$ and $Mn_{1.8}Ge_{0.6}Fe_{3.2}Si_{2.4}$ at 20K.

Chapter Seven   Conclusion and Outlook

7.1 Conclusions

The polycrystalline samples in the pseudo-binary system $(Mn_5Ge_3)_x(MnFe_4Si_3)_{1-x}$ with $x =$ (0.2, 0.4, 0.6, 0.8) were prepared using cold crucible induction melting. Chemical analysis was performed with a iCAP 7600 ICP-OES. The chemical analysis confirmed that the synthesis process was going well, and only small discrepancies from ideal values are observed. In particular, all samples have shown a slight deficiency of Germanium, and the first two samples show a small increase in Manganese content.

Powder XRD at room temperature was performed to investigate the crystal structures of these magnetocaloric compounds, using two types of diffractometers; a Huber G670 diffractometer and PW1050 diffractometer. Using the LeBail method, two phases were detected in all samples. Parts of the pattern showed very few additional weak peaks that were detected after refinement, and that correspond to an impurity phase.

The lattice parameters and unit cell volumes decrease with decreasing x parameter in the two phases, i.e. increasing in Fe and Si. However, an unusually large value is observed at $x = 0.2$ for one of the phases. The c/a ratio remains almost constant for the two phases indicating a uniform contraction of the unit cell volume.

The unit cell volumes indicate that for all sample compositions, at least one of the phases incorporated Ge. For two of the samples ($x = 0.8$ and 0.6) – at least – the second phase incorporated Germanium too. The Rietveld refinement showed that the polycrystalline samples $x = 0.8$ and 0.6 have a preferred orientation in the direction [0 0 1]. The samples with $x = 0.8$ and $x = 0.6$ crystallize in the space group $P6_3/mcm$.

The ratios of Ge to Si obtained from the Rietveld refinement are different from the ones gained from chemical analysis. For the two samples with $x = 0.8$ and $x = 0.6$, the ratios from Rietveld refinement and chemical analysis differ by more than 40% (see Table 6.10).

Mass magnetization measurements for the compounds in the system $(Mn_5Ge_3)_x(MnFe_4Si_3)_{1-x}$ with $x =$ (0.2, 0.4, 0.6, 0.8) were performed using a PPMS. All samples showed a thermal hysteresis. The transitions are observed at temperatures slightly above the room temperature. The transition temperature varies with composition, featuring a maximum at around 331 K for field cooling and around 337 K for field warming for the $x = 0.6$ composition. The thermal hysteresis indicates the character of first order phase transitions. All samples exhibit a thermal hysteresis of approximately 5 K between cooling and heating. Due to the fact that the resulting effective paramagnetic moment is significantly larger than

the spin-only moment, expected from Mn or Fe, we conclude that we are not yet in the Curie-Weiss regime.

7.2 Outlook

Additional isofield magnetization measurements for the studied samples, are needed at high temperatures to reach the Curie-Weiss region. Further isothermal magnetization study is needed to obtain MCE using indirect method. Determination of the MCE using the direct method would be interesting, especially if compared with the results from indirect method.

Powder diffraction data suitable for Rietveld refinements have to be measured on the two missing samples to complete the picture on the structures of the two phases in each of the synthesized samples. In addition, due to the observed discrepancies between the resulting Ge/Si ratio from chemical analysis and the Rietveld refinement, respectively, which might be related to the insufficient quality of the powder diffraction data, it would be desirable to perform powder diffraction experiments at synchrotron and neutron facilities. This would not only allow to obtain data of higher quality, but – due to the high contrast of Mn and Fe in neutron diffraction – the neutron data would also give access to the Mn/Fe ratio of the observed phases.

Mass magnetization measurement may need repetition on the first sample ($x = 0.8$), because the saturation magnetization value is twice the value of the other samples. This, will determine whether an error was made during the experiment or not. In addition, performing elastic and inelastic neutron measurements is needed to get detailed information about compound properties.

The synthesis of single crystals from the polycrystalline samples is important, as this would open a wide range of experimental methodologies. However, prior to a single crystal synthesis, the conditions need optimization to yield a one-phase product.

Bibliography

1. **[Aprea *et al*., 2015]** C. Aprea, A. Greco, A. Maiorino and C. Masselli, *Magnetic refrigeration: an eco-friendly technology for the refrigeration at room temperature*, Journal of Physics: Conference Series, 655, 012026 (2015).

2. **[Ashcroft and Mermin, 1976]** Neil W. Ashcroft and N. David Mermin, *Solid State Physics*, Harcourt, Inc., United States of America (1976).

3. **[Beyss and Gier, 2014]** M. Beyss and H. Gier, Forschungszentrum Jülich GmbH (2014).

4. **[Binczycka *et al*., 1973]** H. Binczycka, Z. Dimitrijevic, B. Gajidand, A. Szytuu, *Atomic and Magnetic Structure of $Mn_{5-x}Fe_xSi_3$*, physica status solidi, 19, K13-K17 (1973).

5. **[Blundell, 2001]** Stephen Blundell, *Magnetism in Condensed Matter*, Oxford University Press Inc., United States (2001).

6. **[Brock *et al*., 2017]** Jeffrey Brock, Nathanael Bell-Pactat, Hong Cai, Timothy Dennison, Tucker Fox, Brandon Free, Rami Mahyub, Austin Nar, Michael Saaranen, Tiago Schaeffer and Mahmud Khan, *The Effect of Fe Doping on the Magnetic and Magnetocaloric Properties of $Mn_{5-x}Fe_xGe_3$*, Advances in Materials Science and Engineering, Volume 2017 (2017).

7. **[Brown, 1976]** G. V. Brown, *Magnetic heat pumping near room temperature*, Journal of Applied Physics, 47, 3673 (1976).

8. **[Brück, 2005]** Ekkes Brück, *Developments in magnetocaloric refrigeration*, Journal of Physics D: Applied Physics, 38, R381–R391 (2005).

9. **[Brückel *et al*., 2018]** Th. Brückel, S. Förster, G. Roth and R. Zorn, *Neutron Scattering*, Jülich Forschungszentrum (2018).

10. **[Cagliotti *et al*., 1958]** G. Cagliotti, A. Paoletti and F. P. Ricci, *Choice of collimators for a crystal spectrometer for neutron diffraction*, Nuclear Instruments 3, 223-228 (1958).

11. **[Candini *et al*., 2004]** A. Candini, O. Moze, W. Kockelmann, J. M. Cadogan, E. Brück, and O. Tegus, *Revised magnetic phase diagram for $Fe_xMn_{5-x}Si_3$ intermetallics*, Journal of Applied Physics, 95, 6819-6821 (2004).

12. **[Carroll *et al*., 2017]** Patrick Carroll, Amber Williams, Miranda Caudle, Lindsay Darkins, Adam Eaton, Barrett Fitzgerald, Brian Knauf, Matthew Rurka, Eli Shlonsky, Paul Wilson and Jeffrey Brock, Mahmud Khan, *Enhanced magnetic refrigeration capacities in minutely Co doped $Mn_{5-x}Co_xGe_3$ compounds.*

13. **[Charles *et al*., 2004]** Charles B. Boss and Kenneth J. Fredeen, *Concepts, Instrumentation and Techniques in Inductively Coupled Plasma Optical Emission Spectrometry*, PerkinElmer, Inc., USA (2004).

14. **[Chaudhary *et al*., 2019]** V Chaudhary, X Chen and R.V Ramanujan, *Iron and Manganese based Magnetocaloric Materials for Near Room Temperature Thermal Management*, Progress in Materials Science (2018).

15. **[Chen *et al*., 2009]** J. Chen, B. G. Shen, Q. Y. Dong, F. X. Hu and J. R. Sun, *Large reversible magnetocaloric effect caused by two successive magnetic transitions in ErGa compound*, Applied Physics Letters, 95, 132504 (2009).

16. **[Ciszewski, 1963]** R. Ciszewski, *Magnetic Structure of the Mn_5Ge_3 Alloy*, Phys. Stat. Sol., 3, 1999-2004 (1963).

17. **[Cullity, 1978]** B. D. Cullity, *Elements of X-ray diffraction*, Addison-Wesley Publishing Company, Inc., California (1978).

18. **[Cullity and Graham, 2009]** B. D. Cullity and C. D. Graham, _Introduction to magnetic materials_, A John & and Sons Inc., Publication, USA (2009).

19. **[Dan'kov _et al._, 1997]** S. Y. Dan'kov, A. M. Tishin, V. K. Pecharsky and K. A. Gschneidner Jr., _Experimental device for studying the magnetocaloric effect in pulse magnetic fields_, Review of Scientific Instruments, 68, 2432 (1997).

20. **[David _et al._, 2002]** W. I. F. David, K. Shankland, L. B. McCusker and Ch. Baerlocher, _Structure Determination from Powder Diffraction Data_, Oxford, UK (2002).

21. **[Debye, 1926]** P. Debye, _Einige Bemerkungen zur Magnetisierung bei tiefer Temperatur_, Annalen der Physik, 81, 1154-1160 (1926).

22. **[Dinnebier and Billinge, 2008]** Robert E. Dinnebier and Simon J. L. Billinge, _Powder Diffraction: Theory and Practice_, RSC, UK (2008).

23. **[Dollase, 1986]** W. A. Dollase. _Correction of Intensities for Preferred Orientation in Powder Diffractometry: Application of the March Model_, J. Appl. Cryst., 19, 267–72 (1986).

24. **[Forsyth and Brown, 1990]** J B Forsyth and P J Brown, _The spatial distribution of magnetisation density in Mn_5Ge_3_, J. Phys.: Condens. Matter 2, 2713-2720 (1990).

25. **[Franco _et al._, 2012]** V. Franco, J. S. Blazquez, B. Ingale, and A. Conde, _The Magnetocaloric Effect and Magnetic Refrigeration Near Room Temperature: Materials and Models_, Annu. Rev. Mater. Res., 42, 305–342 (2012).

26. **[Földeàki _et al._, 1995]** M. Földeàki, R. Chahine, and T. K. Bose, _Magnetic measurements: A powerful tool in magnetic refrigerator design_, Journal of Applied Physics, 77, 3528 (1995).

27. **[Giauque, 1927]** W.F. Giauque, _A thermodynamic Treatment of Certain Magnetic Effects.A proposed Method of Producing Temperatures Considerably Below1° Absolute_, American Chemical Society, 49, 1864-1870 (1927).

28. **[Giauque and MacDougall, 1933]** W. F. Giauque and D. P. MacDougall, _Attainment of Temperatures Below 1° Absolute by Demagnetization of $Gd_2(SO_4)_3.8H_2O$_, Physical Review, 43, 768 (1933).

29. **[Gschneidner Jr. and Pecharsky, 1999]** K. A. Gschneidner and V. K. Pecharsky, _Magnetic refrigeration materials_, Journal of Applied Physics, 85, 5365-5368 (1999).

30. **[Gschneidner Jr., _et al._, 2005]** K A Gschneidner Jr.,V K Pecharsky and A O Tsokol, _Recent developments in magnetocaloric materials_, Rep. Prog. Phys. 68, 1479–1539 (2005).

31. **[Gottschlich, 2013]** Michael Gottschlich, _Structure, magnetism and excitations in some Mn-based magnetocaloric effect compounds_, Doctoral Thesis, Forschungszentrum Jülich GmbH, Zentralbibliothek (2013).

32. **[Gopal _et al._, 1997]** B. R. Gopal, R. Chahine and T. K. Bose, _A sample translatory type insert for automated magnetocaloric effect measurements_, Review of Scientific Instruments, 68, 1818 (1997).

33. **[Glorieux _et al._, 1996]** C. Glorieux, J. Caerels and J. Thoena, _Magnetic phase transition of gadolinium studied by acoustically detected magnetocaloric effect_, Journal of Applied Physics, 80, 3412 (1996).

34. **[Gombert _et al._, 2002]** Dirk Gombert, John Richardson, Albert Aloy and Delbert Day, _Cold Crucible Design Parameters for Next Generation HLW Melters_, WM'02 Conference, Tucson, AZ (2002).

35. **[Guinebretiere, 2007]** Rene Guinebretiere, _X-ray Diffraction by Polycrystalline Materials_, ISTE, USA (2007).

36. **[Halder *et al*., 2011]** Madhumita Halder, S. M. Yusuf and A. K. Nigam, *Magnetocaloric effect and its implementation in critical behavior study of $Mn_4FeGe_{3-x}Si_x$ intermetallic compounds*, Journal of Applied Physics 110, 113915 (2011).

37. **[Hering et. al., 2015]** P. Hering, K. Friese, J. Voigt, J. Perßon, N. Aliouane, A. Grzechnik, A. Senyshyn, and T. Brückel, *Structure, Magnetism, and the Magnetocaloric Effect of $MnFe_4Si_3$ Single Crystals and Powder Samples*, Chemistry of Materials, 27, 7128-7136 (2015).

38. **[Herlitschke *et al*., 2016]** M. Herlitschke, B. Klobes, I. Sergueev, P. Hering, J. Perßon, and R. P. Hermann, *Elasticity and magnetocaloric effect in $MnFe_4Si_3$*, Physical Review B, 93, 094304 (2016).

39. **[http://pd.chem.ucl.ac.uk]** Department of Chemistry, University College London, United Kingdom.

40. **[http://www.ald-dynatech.com]** Manufacturer of vacuum heat treatment furnace systems, Germany.

41. **[https://www.thermofisher.com]** Biotechnology product development company, Commonwealth of Massachusetts, USA.

42. **[http://www.xhuber.de]** Huber Diffraktionstechnik GmbH Company, Germany.

43. **[Jeppesen *et al*., 2008]** S. Jeppesen, S. Linderoth, N. Pryds, L. Theil Kuhn and J. Buch Jensen, *Indirect measurement of the magnetocaloric effect using a novel differential scanning calorimeter with magnetic field*, Review of Scientific Instruments, 79, 083901 (2008).

44. **[Jiles, 1991]** David Jiles, *Introduction to Magnetism and Magnetic Materials*, Springer-Science + Business Media, B. V., India (1991).

45. **[Johnson *et al*.,1972]** V. Johnson, J. F. Weiher, C. G. Frederick and D. B. Rogers, *Magnetic and Mössbauer effect studies of Mn_5Si_3: Fe_5Si_3 solid solutions*, Journal of Solid State Chemistry, 4, 311-323 (1972).

46. **[Kappel *et al*. 1976]** G. Kappel, G. Fisher and A. Jasglb, *Magnetic Investigation of the System Mn_5Ge_3-Mn_5Si_3*, Phys. Stat. Sol. (a), 34, **691**-696 (1976).

47. **[Khalaniya and Shevelkov, 2019]** Roman A. Khalaniya and Andrei V. Shevelkov, *When two is enough: On the origin of diverse crystal structures and physical properties in the Fe-Ge system*, Journal of Solid State Chemistry (2018).

48. **[Khovaylo *et al*., 2014]** Vladimir V. Khovaylo, Valeria V. Rodionova, Sergey N. Shevyrtalov, and Val Novosad, *Magnetocaloric effect in "reduced" dimensions: Thin films, ribbons, and microwires of Heusler alloys and related compounds*, Physica Status Solidi B, 1–10 (2014).

49. **[Kim *et al*., 2015]** Yongdeok Kim, Ki Hoon Kang, Ju Hwan Kim, Eun Jeong Kim, Kwangseok Choi, Won Bae Han, Hee-Soo Kim, Yoong Oh and Chong Seung Yoon, *Magnetocaloric refrigerant with wide operating temperature range based on $Mn_{5-x}Ge_3(Co, Fe)_x$ composite*, Journal of Alloys and Compounds, 644, 464–469 (2015).

50. **[Krawitz, 2001]** Aaron D. Krawitz, *Introduction to Diffraction in Materials Science and Engineering*, Wiley, New York (2001).

51. **[Kuz'min and Tishin, 1992]** M. D. Kuz'min and A. M. Tishin, *Magnetocaloric effect. Part 1: An introduction to various aspects of theory and practice*, Cryogenics, Vol 32, No 6, 545-558 (1992).

52. **[Ladd and Palmer, 2013]** Mark Ladd and Rex Palmer, *Structure Determination by X-ray Crystallography*, Springer, New York (2013).

53. **[Lander *al*., 1967]** G. H. Lander, P. J. Brown and J. B. Forsyth, *The antiferromagnetic structure of Mn_5Si_3*, Proceedings of the Physical Society, 91, 332-340 (1967).

54. **[Levitin *et al*., 1997]** R. Z. Levitin, V. V. Snegirev, A. V. Kopylov, A. S. Lagutin, A. Gerber, *Magnetic method of magnetocaloric effect determination in high pulsed magnetic fields*, Journal of Magnetism and Magnetic Materials, 170, 223-227 (1997).

55. **[Le Bail *et al*., 1988]** D. H. Le Bail, A. and J. L. Fourquet, *Ab-initio structure determination of $LiSbWO_6$ by X-Ray powder* diffraction, Materials Research Bulletin, 23, 447-452 (1988).

56. **[Liu and Altounian, 2006]** X. B. Liu, and Z. Altounian, *Magnetocaloric effect in $Mn_5Ge_{3-x}Si_x$ pseudobinary compounds*, Journal of Applied Physics, 99, 08Q101 (2006).

57. **[March, 1932]** Artur March**,** *Mathematische Theorie der Regelung nach der Korngestah bei affiner Deformation*, Zeitschrift Für Kristallographie - Crystalline Materials, 81, 285-297 (1932).

58. **[McCusker, *et al*., 1999]** L. B. McCusker, R. B. Von Dreele, D. E. Cox, D. Loueer and P. Scardi, *Rietveld refinement guidelines*, J. Appl. Cryst. 32, 36-50 (1999).

59. **[Menshikov *et al*., 1990]** A. Z. Menshikov, A. P. Vokhmyanin, and Yu. A. Dorofeev, *Magnetic Structure and Phase Transformaiions in Mn_5Si_3*, Phys. Stat. Sol., (b) 158, **319-328** (1990).

60. **[Morawiec and Stróz, 2004]** Henryk Morawiec and Danuta Stróz, *Applied Crystallography*, World Scientific Publishing Co. Pte. Ltd, New Jersy (2004).

61. **[Mühlbauer, 2006]** A. Mühlbauer, *Innovative Induction Melting Technologies: A Historical Review*, International Scientific Colloquium, Modelling for Material Processing, Riga (2006).

62. **[Ohoyama, 1961]** Tetuo Ohoyama, *X-ray and Magnetic Studies of the Manganese-Germanium System*, Journal of the Physical Society of Japan, 16, 1995-2002 (1961).

63. **[Otowski *et al*., 1993]** W. Otowski, C. Glorieux, R. Hofman and J. Thoen, *New acoustic detection technique for a magnetocaloric effect*, Thermochimica Acta, 218, 123-133 (1993).

64. **[Pecharsky and Gschneidner Jr., 1999[(1)]]** V. K. Pecharsky and K. A. Gschneidner Jr., *Magnetocaloric effect from indirect measurements: Magnetization and heat capacity*, Journal of Applied Physics, 86, 565-575 (1999).

65. **[Pecharsky and Gschneidner Jr., 1999[(2)]]** V. K. Pecharsky and K. A. Gschneidner Jr., *Heat capacity near first order phase transitions and the magnetocaloric effect: An analysis of the errors, and a case study of $Gd_5(Si_2Ge_2)$ and Dy*, Journal of Applied Physics, 86, 6315 (1999).

66. **[Pecharsky and Gschneidner Jr., 1999[(3)]]** Vitalij K. Pecharsky, Karl A. Gschneidner Jr., *Magnetocaloric effect and magnetic refrigeration*, Journal of Magnetism and Magnetic Materials, 200, 44-56 (1999).

67. **[Pecharsky and Gschneidner Jr., 1997]** V. K. Pecharsky and K. A. Gschneidner Jr., *Giant Magnetocaloric Effect in $Gd_5(Si_2Ge_2)$*, Physical Review Letters, 78, 4494 (1997).

68. **[Pecharsky and Zavalij, 2005]** Vitalij K. Pecharsky and Peter Y. Zavalij, *Fundamentals of powder diffraction and structural characterization of materials*, Springer, New York (2005).

69. **[Pericleous *et al*., 2006]** K. Pericleous, V. Bojarevics, G. Djambazov, R.A. Harding, M. Wickins, *Experimental and numerical study of the cold crucible melting process*, Applied Mathematical Modelling 30, 1262–1280 (2006).

70. **[Petříček *et al*., 2014]** Václav Petříček, Michal Dušek and Lukáš Palatinus, *Crystallographic Computing System JANA2006: General features*, Z. Kristallogr, 229(5), 345–352 (2014).

71. **[Porcari *et al*., 2013]** G. Porcari, M. Buzzi, F. Cugini, R. Pellicelli, C. Pernechele, L. Caron, E. Brück and M. Solzi, *Direct magnetocaloric characterization and simulation of thermomagnetic cycles*, Review of Scientific Instruments, 84, 073907 (2013).

72. **[Qiu, 2014]** Yue Qiu, *The elastic properties of $MnFe_4Si_3$ and Mn_4FeSi_3 measured with Resonant Ultrasound Spectroscopy*, Bachelor Thesis, Forschungszentrum Jülich GmbH (2014).

73. **[Quintana *et al.*, 2011]** I. Quintana, Z. Azpilgain, D. Pardo and I. Hurtado, *Numerical Modeling of Cold Crucible Induction Melting*, *Excerpt from the Proceedings of the 2011 COMSOL Conference in Stuttgart* (2011).

74. **[Ramos *et al.,* 2002]** M Ramos Silva, P J Brown and J B Forsyth, *Magnetic moments and magnetic site susceptibilities in Mn_5Si_3*, J. Phys.: Condens. Matter, 14, 8707–8713 (2002).

75. **[Rietveld, 1967]** H. M. Rietveld, *Line profiles of neutron powder-diffraction peaks for structure refinement*, Acta Cryst. 22, 151-152 (1967).

76. **[Rudowicz and Sung, 2003]** C. Rudowicz and H. W. F. Sung, *Textbook treatments of the hysteresis loop for ferromagnets-Survey of misconceptions and misinterpretations*, American Journal of Physics, 71, 1080-1083 (2003).

77. **[Singal *et al.*, 2016]** Dr. L. C. Singal, Aishna Mahajan and Rajwinder Singh, *Magnetic Refrigeration- A Review- A boon for the coming generations*, International Journal of Mechanical Engineering, volume 3, Issue 5, 46-52 (2016).

78. **[Skomski *et al.* 2018]** R. Skomski, P. Kumar, B. Balamurugan, B. Das, P. Manchanda, P. Raghani, A. Kashyap and D.J. Sellmyer, *Exchange and magnetic order in bulk and nanostructured Fe_5Si_3*, Journal of Magnetism and Magnetic Materials, 460,438–447 (2018).

79. **[Smith *et al.*, 2012]** Anders Smith, Christian R. H. Bahl, Rasmus Bjørk, Kurt Engelbrecht, Kaspar K. Nielsen and Nini Pryds, *Materials Challenges for High Performance Magnetocaloric Refrigeration Devices*, Advanced energy materials (2012).

80. **[Sochi, 2010]** Taha Sochi, *High Throughput Software for Powder Diffraction and its Application to Heterogeneous Catalysis*, Doctoral Thesis, The Department of Crystallography, Birkbeck College London (2010).

81. **[Songlin *et al.*, 2002$^{(1)}$]** Songlin, Dagula, O. Tegus, E. Brück, F. R. de Boer and K. H. J. Buschow, *Magnetic and magnetocaloric properties of $Mn_5Ge_{3-x}Sb_x$*, Journal of Alloys and Compounds, 337, 269–271 (2002).

82. **[Songlin *et al.*, 2002$^{(2)}$]** Songlin, Dagula, O. Tegus, E. Brück, J. C. P. Klaasse, F. R. de Boer and K. H. J. Buschow, *Magnetic phase transition and magnetocaloric effect in $Mn_{5-x}Fe_xSi_3$*, Journal of Alloys and Compounds, 334, 249–252 (2002).

83. **[Sun *et al.*, 2017]** Y. W. Sun, J. L. Yan, E. L. Feng, G. W. Tang, K. W. Zhou, *Effect of Fe substitution on the structure and magnetocaloric effect of $Mn_{5-x}Fe_xGeSi_2$ alloys*, Journal of Magnetism and Magnetic Materials, 422, 356–361 (2017).

84. **[Tawara and Sato, 1963]** Yoshio Tawara and Kiyoo Sato, *On the Magnetic Anisotropy of Single Crystal of Mn_5Si_3*, Journal of the Physical Society of Japan, Vol. 18, No. 6, 773-777 (1963).

85. **[Tolinski and Synoradzki, 2014]** T. Tolinski and K. Synoradzki, *Specific heat and magnetocaloric effect of the Mn_5Ge_3 ferromagnet*, Intermetallics, 47, 1-5 (2014).

86. **[Tosun *et al.*, 2018]** Onur Tosun, Mohammed Salehi-Fashami, Balamurugan Balasubramanian, Ralph Skomski, David J. Sellmyer and George C. Hadjipanayis, *Structure and Magnetism of Mn_5Ge_3 Nanoparticles*, Nanomaterials, 8, 241 (2018).

87. **[Vinokurova *et al.*, 1995]** L. Vinokurova, V. Ivanov, E. Kulatov, *Magnetic phase transitions in single crystals of Mn_5Si_3 and $(Mn,Fe)_5Si_3$*, Physica B, 211, 96-98 (1995).

88. **[(VSM) Option User's Manual]** 4th edition of the VSM manual from QuantumDesign, Part Number 1096-100, A3, San Diego, CA 92121, USA (2008).

89. **[Will, 2006]** Georg Will, *Powder Diffraction: The Rietveld Method and the Two Stage Method*, Springer, Germany (2006).

90. **[Windsheimer *et al*., 2015]** Hans Windsheimer, Roland Waitz and Peter Wübben, *Inductive melting in cold wall crucible: technology and applications*, Induction technology report (2015).

91. **[Yusupov *et al*., 2009]** R. G. Yusupov, C. J. Stanley, M. D. Welch, J. Spratt, G. Cressey, M. S. Rumsey, R. Seltmann and E. Igamberdiev, *Mavlyanovite, Mn5Si3: a new mineral species from a lamproite diatreme, Chatkal Ridge, Uzbekistan*, Mineralogical Magazine, 73, 43–50 (2009).

92. **[Zhang *et al*., 2007]** Q. Zhang, J. Du, Y. B. Li, N. K. Sun, W. B. Cui, D. Li and Z. D. Zhang, *Magnetic properties and enhanced magnetic refrigeration in $(Mn_{1-x}Fe_x)_5Ge_3$ compounds*, Journal of Applied Physics, 101, 123911 (2007).

93. **[Zhao *et al*., 2006]** F. Q. Zhao, W. Dagula, O. Tegus and K. H. J. Buschow, *Magnetic-entropy change in $Mn_5Ge_{3-x}Si_x$ alloy*, Journal of Alloys and Compounds 416, 43-45 (2006).

94. **[Zheng *et al*., 2012]** T. F. Zheng, Y. G. Shi, C. C. Hu, J. Y. Fan, D. N. Shi, S. L. Tang and Y. W. Du, *Magnetocaloric effect and transition order of Mn_5Ge_3 ribbons*, Journal of Magnetism and Magnetic Materials 324, 4102–4105 (2012).

Appendix A

Table A.1: Command sequence for magnetization measurements performed on the PPMS which include FC, then Hysteresis measurements at 20 K, then FW and then stabilization of the VSM.

| |
|---|
| New Datafile "file location\ file name.dat" |
| Set Temperature 390K at 10K/min. Fast settle |
| Wait For Temperature, Delay 2 secs, No Action |
| Set Magnetic Field 1000.0Oe at 200.0Oe/sec, Linear, Persistent |
| Wait For Field, Delay 5 secs, No Action |
| VSM Moment vs Temperature 390K to 20K Sweep Continuous AutoCenter ON |
| New Datafile "file location\ file name.dat" |
| Set Magnetic Field 80000.0Oe at 200.0Oe/sec, Linear, Persistent |
| Wait For Field, Delay 5 secs, No Action |
| VSM Moment vs Field 4 Quadrants -80000.0Oe to 80000.0Oe Sweep Continuous AutoCenter ON |
| **New Datafile "file location\ file name.dat"** |
| Set Magnetic Field 1000.0Oe at 200.0Oe/sec, Linear, Persistent |
| Wait For Field, Delay 5 secs, No Action |
| VSM Moment vs Temperature 20K to 390K Sweep Continuous AutoCenter ON |
| Set Temperature 300K at 10K/min. Fast settle |
| Wait For Temperature, Delay 2 secs, No Action |
| Set Magnetic Field 0.0Oe at 200.0Oe/sec, Linear, Persistent |
| Wait For Field, Delay 5 secs, No Action |
| End Sequence |
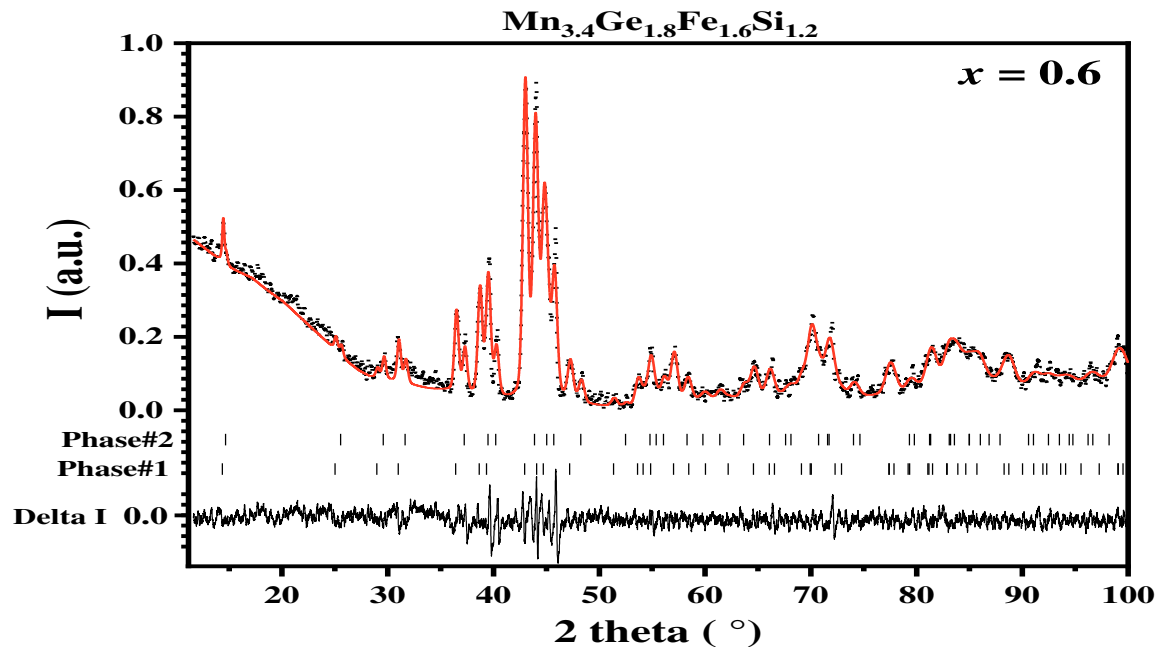
Figure A.1: Observed (black) and calculated (red) profiles using the LeBail method for $Mn_{3.4}Ge_{1.8}Fe_{1.6}Si_{1.2}$ based on the data from the Huber diffractometer.
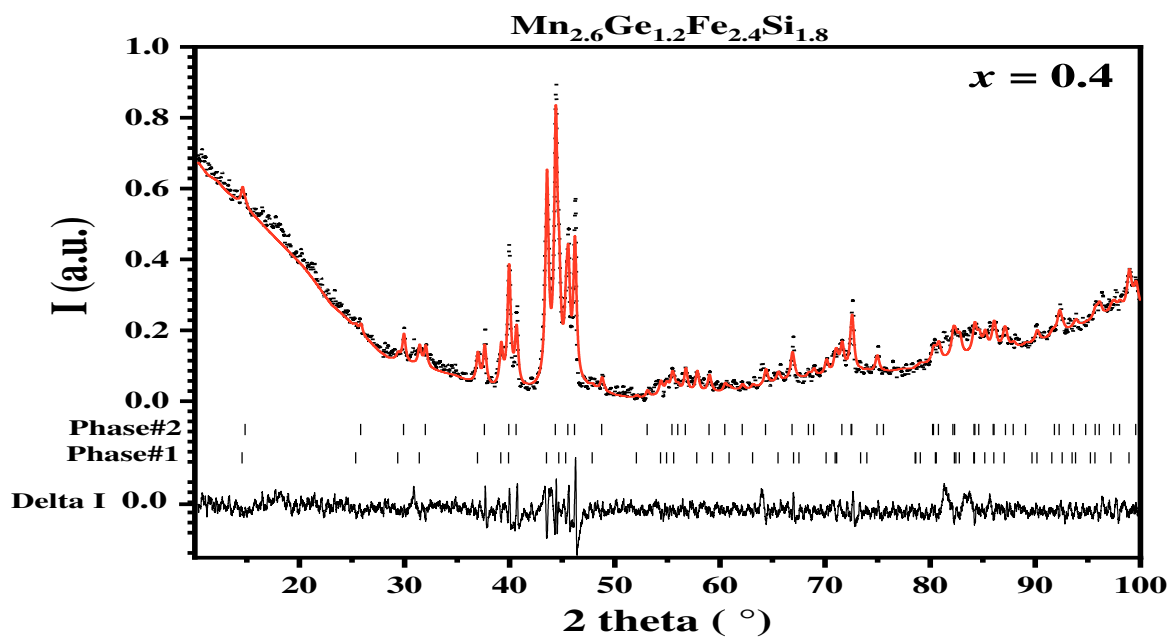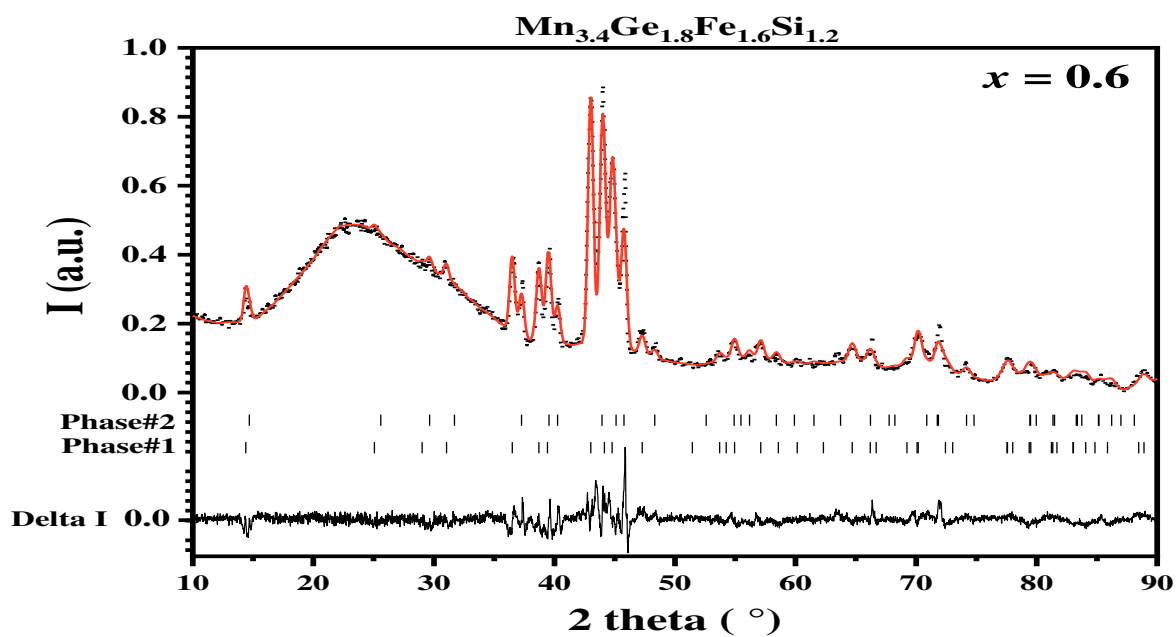
Figure A.2: Observed (black) and calculated (red) profiles using the LeBail method for $Mn_{2.6}Ge_{1.2}Fe_{2.4}Si_{1.8}$ based on the data from the Huber diffractometer.
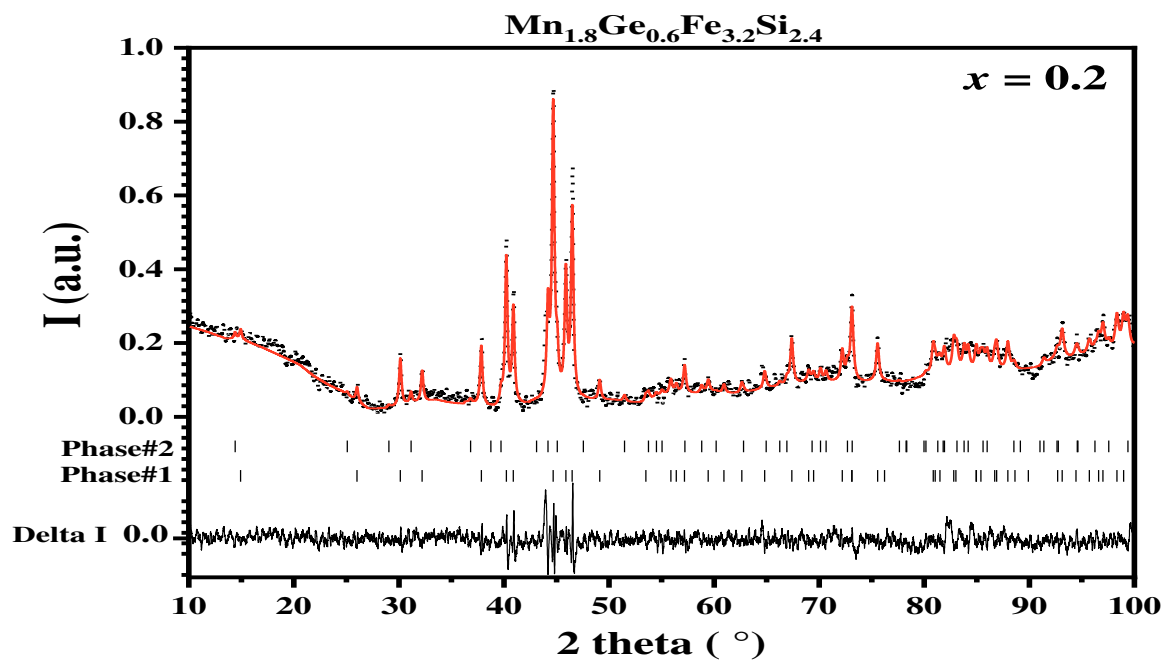
Figure A.3: Observed (black) and calculated (red) profiles using the LeBail method for $Mn_{1.8}Ge_{0.6}Fe_{3.2}Si_{2.4}$ based on the data from the Huber diffractometer.
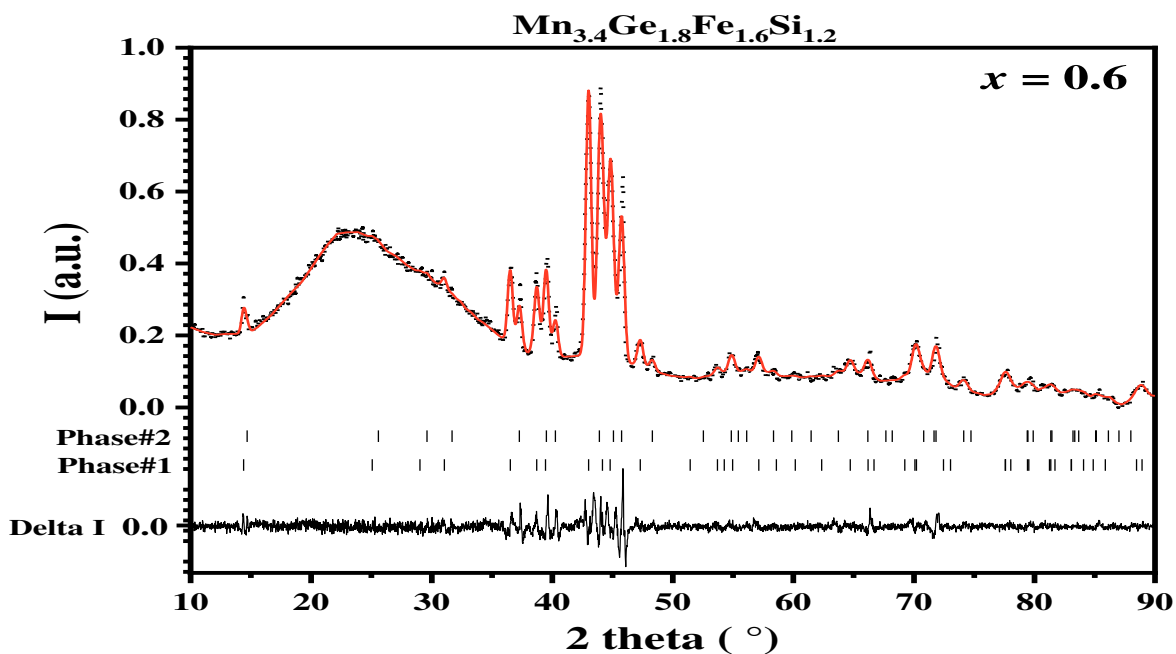
Figure A.4: Observed (black) and calculated (red) profiles using the LeBail method for $Mn_{3.4}Ge_{1.8}Fe_{1.6}Si_{1.2}$ based on the data from the PW1050 diffractometer.

Figure A.5: Observed (black) and calculated (red) profiles using the Rietveld method for $Mn_{3.4}Ge_{1.8}Fe_{1.6}Si_{1.2}$ based on the data from the PW1050 diffractometer.

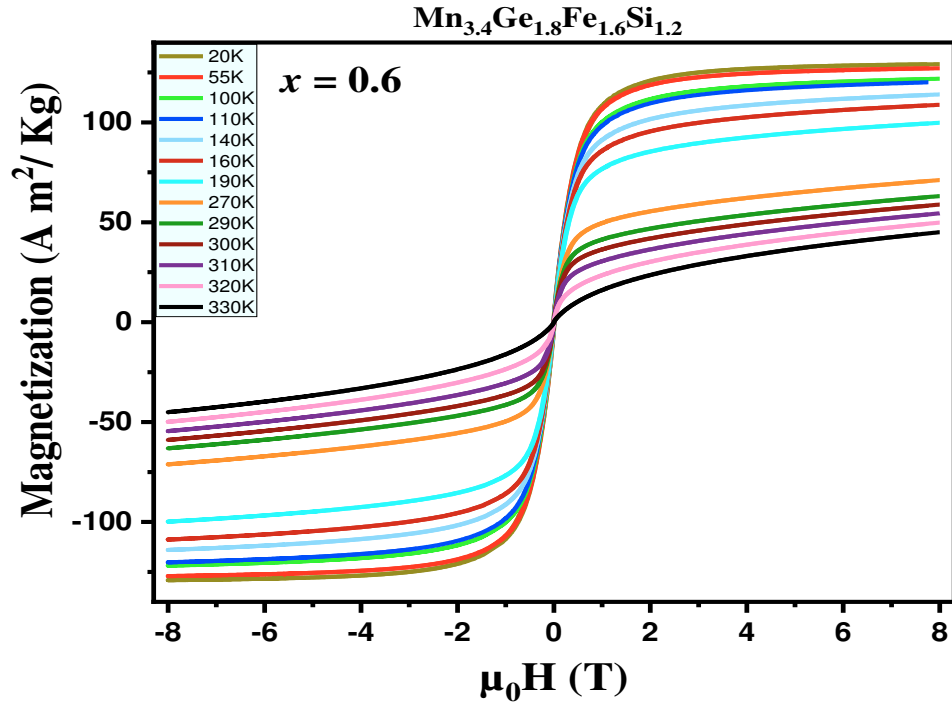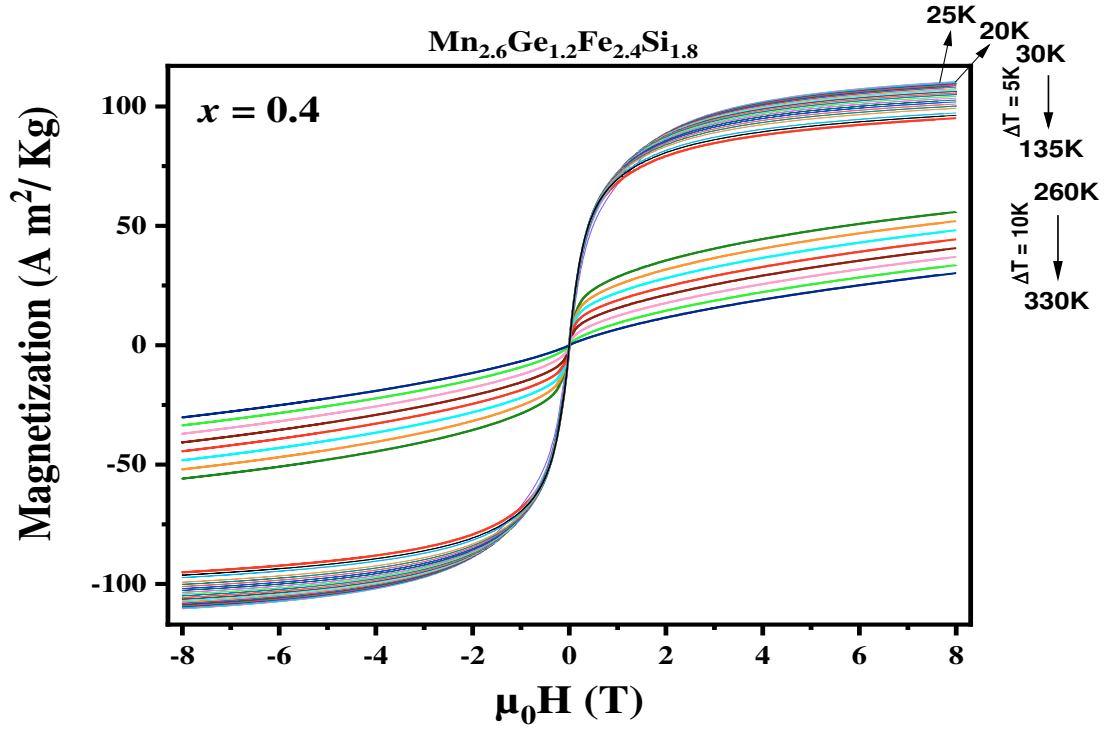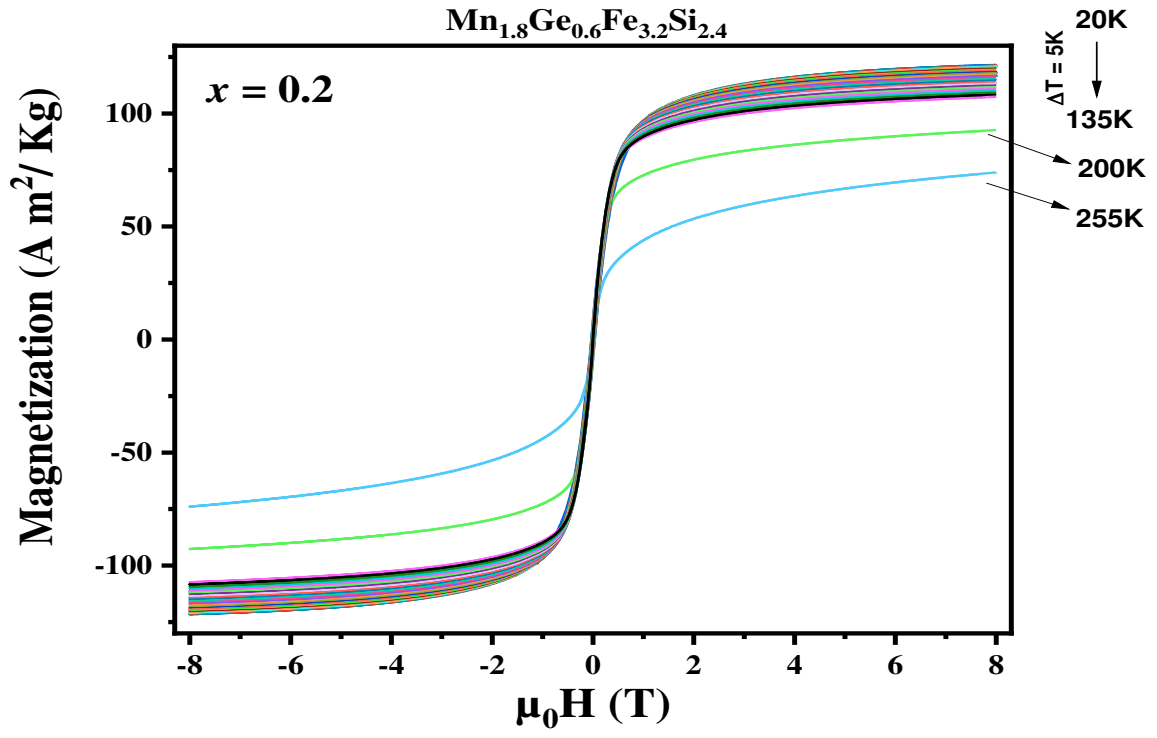**Figure A.6:** Isothermal measurements of magnetization of $Mn_{3.4}Ge_{1.8}Fe_{1.6}Si_{1.2}$ at different temperatures.

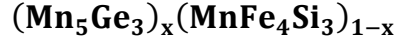**Figure A.7:** Isothermal measurements of magnetization of $Mn_{2.6}Ge_{1.2}Fe_{2.4}Si_{1.8}$ at different temperatures.

Figure A.8: Isothermal measurements of magnetization of $Mn_{1.8}Ge_{0.6}Fe_{3.2}Si_{2.4}$ at different temperatures.

تصنيع ودراسة البنية البلورية والخصائص المغناطيسية للمركب المغناطيسي الحراري $(Mn_5Ge_3)_x(MnFe_4Si_3)_{1-x}$

إعداد: كنان خالد جميل النمورة

إشراف: د. سلمان سلمان و د. كارين فريزي و د. يورغ فويغت

الملخص

تم في هذا البحث تصنيع المركبات المغناطيسية الحرارية في النظام $(Mn_5Ge_3)_x(MnFe_4Si_3)_{1-x}$ بنسب مختلفة ($x = 0.2, 0.4,$ $0.6, 0.8$) حيث تم الصهر باستخدام الحث (Cold crucible induction melting).

بعد ذلك تم تحضير مساحيق من العينات البلورية المصنعة والتأكد من صحة نسب العناصر في المركبات وخلوها من الشوائب عن طريق تحليل كيميائي للعينات باستخدام جهاز (iCAP 7600 ICP-OES). بشكل عام كانت الاختلافات طفيفة فقد أظهرت العينات نقصا قليلا في نسبة عنصر الجيرمانيوم في كل العينات وزيادة طفيفة في نسبة المنغنيز في العينتين الأولى والثانية ($x = 0.6, 0.8$).

وباستخدام حيود الأشعة السينية للمساحيق المحضرة عند درجة حرارة الغرفة وأساليب التنقيح ليبايل وريتفلد (LeBail and Rietveld Refinement) تم تحديد البنية البلورية للعينات. وجد أن جميع العينات تحتوي بشكل رئيسي على طورين وأن حجم وحدة الخلية (unit cell) في الطورين يتناقص مع زيادة معامل نسبة العناصر في المركب x، ما عدا العينة الرابعة ($x = 0.2$) التي أظهرت عكس ذلك حيث بقيت النسبة (c/a) ثابتة تقريبا للطورين في جميع العينات مما يشير إلى تقلص عام لحجم وحدة الخلية. وقد أظهر تنقيح ريتفلد أن الاتجاه التفضيلي لجميع البلورات هو [1 0 0] و أن الزمرة الفراغية للعينتين الأولى والثانية ($x = 0.8, 0.6$) هي $P6_3/mcm$. يشير حجم وحدة الخلية إلى أن الطور الأول يحتوي على عنصر الجرمانيوم في جميع العينات كما يحتوي الطور الثاني على عنصر الجرمانيوم في العينتين الأولى والثانية ($x = 0.8, 0.6$) على الأقل.

تم اختبار الخصائص المغناطيسية للعينات باستخدام جهاز (PPMS) خيار (VSM). واستخدم المجال المغناطيسي بقيم ما بين -8 تسلا إلى +8 تسلا في حالة قياس المغنطة مع ثبوت درجات الحرارة (Isothermal magnetization measurements). أما في حالة قياس المغنطة مع ثبوت المجال (Isofield magnetization measurements) فكانت قيمته 0.1 تسلا. وكانت درجات حرارة الانتقال بين الأطوار المغناطيسية في حالة قياس المغنطة أثناء تخفيض درجات الحرارة (Field cooling) مختلفة عنها في حالة زيادة درجات الحرارة (Field warming) وينطبق ذلك على جميع العينات، فيما يعرف بـ "التباطؤ المغناطيسي" (Thermal hysteresis).

كما أن درجات الحرارة الانتقالية كانت مختلفة بين عينة و أخرى. وكانت أعلى قيم للعينة الثانية ($x = 0.6$)، حيث كانت درجة الحرارة في حالة قياس المغنطة أثناء تخفيض درجات الحرارة حوالي 331 كلفن، وحوالي 337 كلفن في حالة الزيادة في درجات الحرارة. التباطؤ الحراري يشير إلى حدوث انتقال بين الأطوار المغناطيسية من الدرجة الأولى (First order phase transition). وحيث كان العزم المغناطيسي الفعال للمادة البارامغناطيسية (effective paramagnetic moment) أكبر من القيمة النظرية فإننا لم نصل إلى منطقة كوري- وايس (Curie-Weiss regime).